ESCOLA SUPERIOR DE TECNOLOGIA DA SAÚDE DE LISBOA
INSTITUTO POLITÉCNICO DE LISBOA

Instituto Politécnico de Lisboa

Escola Superior de Tecnologia da Saúde de Lisboa

Influence of the Time-of-Flight and the Acquisition Time on Image Quality in Positron Emission Tomography/Computed Tomography Scanners

Thesis submitted in fulfilment of the requirements to obtain the Master's Degree in Radiations Applied to Health Technologies – specialization area in Multimodal and Functional Imaging

Joana da Fonseca e Oliveira

Lisboa, 2016

Instituto Politécnico de Lisboa

Escola Superior de Tecnologia da Saúde de Lisboa

Influence of the Time-of-Flight and the Acquisition Time on Image Quality in Positron Emission Tomography/Computed Tomography Scanners

Joana da Fonseca e Oliveira

Thesis supervised by:

Susana Oliveira Branco, PhD.

Escola Superior de Tecnologia da Saúde de Lisboa

Rui Miguel Carreiro Mota Parafita, MSc.

Fundação Champalimaud

Jury:

President – Maria João Furtado Raminhas Carapinha, PhD.

Escola Superior de Tecnologia da Saúde de Lisboa

Arguer – Francisco José Cerqueira Alves, PhD.

Escola Superior de Tecnologia da Saúde de Coimbra

Instituto de Ciências Nucleares Aplicadas à Saúde

(This version includes the comments and suggestions made by the jury)

Lisboa, 2016

To my uncle, Fernando Fonseca

Acknowledgments

I would like to thank, firstly, Doctor Durval Costa, for allowing the development of this thesis in the prestigious *Champalimaud Foundation.*

I do not have enough words to express my gratitude to my supervisors Susana Branco and Rui Parafita. To Susana Branco, who was so committed to this thesis as I was, even when she was giving birth (literally). I have to mention this episode (sorry…): after waters break, she remembered we would have a meeting in that afternoon, so she texted me explaining what happened (while she was in her way to the hospital). To Rui Parafita, that spent some Saturday mornings helping me to acquire data, always with joy and sense of humor, no matter what time it was in the morning or if there were some unforeseen during the thesis development. Thank you both so much for your dedication.

I would like to thank Ana Canudo also, for waking so early on these Saturdays just to eluate the ^{68}Ga from the generator and helping us to prepare the activities. If there are people dedicated to their jobs, these are certainly some of them.

To my parents, Helena e João, and my sister, Vera, for their support along this pathway. You are my *rocks*; I could not have done it without you.

To my boyfriend, Sérgio, for encouraging me and always being there, even when he was swamped in both his master's degree and work. Thank you for your fellowship, understanding and love.

Many thanks, Graça, for the *brainstorming* moments about this thesis and also for the chill out moments.

I would like to thank my group of friends (you know who you are) for the shared moments. You know, friends are the family we choose.

At last, I would like to thank to other family, friends, colleagues and professors that I not mention before, but were part of this stage in my life.

Thank you all!

Nothing in life is to be feared, it is only to be understood. Now is the time to understand more, so that we may fear less.

Marie Curie

Resumo

Na Tomografia por Emissão de Positrões (PET) têm sido feitas melhorias significativas para superar a qualidade de imagem, nomeadamente, a incorporação do tempo de voo (TOF) nos tomógrafos. Esta técnica é útil para localizar o ponto de emissão do radiofármaco emissor de positrões (partículas β^+) dentro do organismo, medindo a diferença dos tempos de deteção dos fotões em coincidência. Os equipamentos PET com tecnologia TOF proporcionam uma melhoria na razão sinal-ruído (SNR) e uma diminuição das coincidências aleatórias, permitindo, assim, melhor contraste das lesões, sobretudo em pacientes obesos, e maior detalhe das estruturas, possibilitando ainda menores tempos de aquisição de imagens ou menores atividades administradas.

Os objetivos principais deste estudo consistem em investigar o menor tempo de aquisição, sem comprometer a qualidade de imagem num fantoma de corpo NEMA e determinar como é que isso pode ser traduzido num melhor desempenho nas imagens dos pacientes. Para tal, foram obtidos diferentes tempos de aquisição por posição da *bed* (30, 45, 60, 80 e 120 s) num tomógrafo PET/Tomografia Computadorizada (PET/CT) com TOF integrado (GEMINI TF 16, Philips), utilizando citrato de Gálio-68 (^{68}Ga). A aquisição de um paciente aleatório (masculino, 64 anos) foi realizada com ^{68}Ga-Antigénio da membrana específica da próstata (^{68}Ga-PSMA). Parâmetros de qualidade de imagem, como ruído, SNR, contraste, razão contraste-ruído (CNR), coeficiente de contraste recuperado (CRC), coeficiente de volume recuperado (VRC) e ainda quantificação em termos de valor de captação estandardizado (SUV) foram obtidos. O aumento do contraste em esferas maiores e com tempos de aquisição mais longos produz um aumento no ruído do sinal, levando a uma diminuição da SNR e da CNR. Nas imagens do fantoma, o SUV_{max} variou entre 1,1 e 1,6 para o fundo (captações normais) e entre 2,1 e 8,0 para as esferas (captações anómalas). Foram encontradas diferenças estatisticamente significativas ($p < 0,05$) entre os tempos mais curtos e os mais longos para o SUV_{max} e apenas entre o tempo mais curto e os restantes tempos de aquisição para o $SUV_{médio}$. Nas imagens do paciente, os valores de SNR, contraste, ruído e CNR foram superiores no baço, comparativamente ao fígado. O SUV_{max} médio foi 7,1 para o fígado; 9,8 para baço e 1,8 para o osso. Para futuras práticas clínicas, um tempo entre 45 e 60 s por posição da *bed* é proposto, permitindo a marcação de mais exames por dia, contribuindo para uma otimização dos protocolos sem comprometer a qualidade de imagem.

Palavras-chave: PET/CT; TOF; ^{68}Ga; tempo de aquisição; qualidade de imagem.

Abstract

Significant improvements have been made in Positron Emission Tomography (PET) to enhance the image quality, namely, the development of time-of-flight (TOF) technology. This technique is useful to localize the emission point of the beta plus-emitter (β^+) radiopharmaceutical inside the body, by measuring the difference in coincident photon detection times. TOF PET scanners enable an improvement signal-to-noise ratio (SNR) and decrease of random coincidences, allowing better lesion contrast, especially for large patients, improving structural details and leading to a short scan time or injected dose.

The main goals of this study are to investigate the shortest acquisition time without compromising the image quality in a NEMA body phantom and to determine how it translates into improved performance for patient imaging. For that purpose, different acquisition times per bed position (30, 45, 60, 80 and 120 s) were achieved in a TOF PET/Computed Tomography (PET/CT) scanner (GEMINI TF 16, Philips), using Gallium-68 (^{68}Ga) citrate. Acquisition of an aleatory patient (male, 64 years old) was also performed with ^{68}Ga-Prostate specific membrane antigen (^{68}Ga-PSMA). Image quality parameters, such as noise, SNR, contrast, contrast-to-noise ratio (CNR), contrast recovery coefficient (CRC), volume recovery coefficient (VRC) and also quantification in terms of standardized uptake value (SUV) were acquired. The increased contrast in larger spheres and with longer acquisition times produces an increase on the noise of the mean signal recover, leading to a decrease in SNR and CNR. In phantom imaging, SUV_{max} varied between 1.1 and 1.6 for background (normal uptake) and between 2.1 and 8.0 for spheres (abnormal uptake). There were statistically significant differences ($p < 0.05$) between shorter and longer acquisition times for SUV_{max} and between only the shorter acquisition time and the rest of acquisition times for SUV_{mean}. In patient imaging, spleen showed higher SNR, contrast, noise and CNR than liver. Median SUV_{max} was 7.1 for liver, 9.8 for spleen and 1.8 for bone. A time between 45 and 60 s per bed position is proposed for future clinical practices, allowing schedule more scans per day, contributing to an optimization of protocols without compromising the image quality.

Keywords: PET/CT; TOF; ^{68}Ga; acquisition time; image quality.

Contents

List of tables

List of figures

List of abbreviations and symbols

AC	Attenuation Correction
ACF	Attenuation Correction Factors
AMIDE	A Medical Image Data Examiner
ART	Algebraic Reconstruction Techniques
BaF_2	Barium Fluoride
^{11}C	Carbone-11
CdTe	Cadmium Telluride
CNR	Contrast-to-Noise Ratio
Cps	Counts per second
CRC	Contrast Recovery Coefficient
CT	Computed Tomography
CTAC	CT-based attenuation correction
CZT	Cadmium Zinc Telluride
^{18}F	Fluorine-18
^{18}F-FDG	^{18}F-fluorodeoxyglucose
FBP	Filtered Back-Projection
FOV	Field Of View
FWHM	Full Width at Half Maximum
^{68}Ga	Gallium-68
^{68}Ga-PSMA	^{68}Ga-Prostate Specific Membrane Antigen
Ge	Germanium
HCl	Hydrochloric acid
IEC	International Electrotechnical Commission
$LaBr_3$	Lanthanum Bromide
LOR	Line Of Response
LSO	Lutetium OxyorthoSilicate
LYSO	Lutetium-Yttrium OxyorthoSilicate
MAP	Maximum *A Posteriori*
ML	Maximum Likelihood
MLEM	Maximum Likelihood Expectation-Maximisation
^{13}N	Nitrogen-13
NaCl	Sodium Chloride

NaI(Tl)	Sodium Iodide doped with Thallium
NEMA	National Electrical manufacturers Association
^{15}O	Oxygen-15
OSEM	Ordered Subset Expectation Maximisation
PE	Percentage Error
PET	Positron Emission Tomography
PET/CT	Positron Emission Tomography/Computed Tomography
PET/MRI	Positron Emission Tomography/Magnetic Resonance Imaging
PHA	Pulse Height Analyser
PMTs	PhotoMultiplier Tubes
PSF	Point Spread Function
PVC	Partial Volume Correction
PVE	Partial Volume Effect
RAMLA	3D Row Action Maximum Likelihood Algorithm
ROI	Region Of Interest
Si	Silicon
SI	*Système International (d'unités)*
SnO_2	Tin dioxide
SNR	Signal-to-Noise Ratio
SPECT	Single-Photon Emission Computed Tomography
SUV	Standardized Uptake Value
TiO_2	Titanium dioxide
TOF	Time-Of-Flight
VOI	Volume Of Interest
VRC	Volume Recovery Coefficient
Z	Atomic number
3D	3-dimensional
α	Alfa particle
β^+	Positron (Beta plus particle)
γ	Gamma photon
μ	Linear attenuation coefficient
Δt	Timing resolution
σ	Standard deviation

Chapter I – Introduction

1. Introduction

In the early 1990s, the proposal to combine Positron Emission Tomography (PET) with Computed Tomography (CT) was made, improving the staging of malignant diseases, monitoring and evaluation of response to therapeutic (1).

One of the most important progresses in PET was the introduction of Time-Of-Flight (TOF) PET systems on the market in 2006, although it was originally proposed in the 1960s (2). The advantages of the use of TOF PET relate to noise reduction, a higher accuracy in the image, the reduction of radioactivity in each scan (as for the image reconstruction are required less counts) and a shorter acquisition time. But how far can we go? What is the minimum acquisition time per bed position without compromising image quality? There are no protocols about it. Investigations made by other authors indicates that for small and average patients sizes, 1-2 minutes per bed position will translate into a 10 to 20 minutes scan time per patient and lead satisfactory image quality. For heavier patients with increased attenuation, is used 3 minutes per bed position or 30 minutes total scan time (3).

The proposed theme is important in Nuclear Medicine, especially in PET, once most of nuclear medicine scans take a long time of acquisition (sometimes upper than half an hour). This contributes for the discomfort of the patient, increasing the probability of motion and, consequently, generation of artifacts, degrading the image quality. Furthermore, longer acquisition times imply less scans per day and increases the number of patients waiting to do the scan. The motivation to develop this study arises from the need to shorten the scan time and thereby more scans could be scheduled, contributing for an optimization of the protocols. The major aim of this work is to verify the shortest acquisition time per bed position, in a TOF PET scanner, without compromising the image quality (qualitative and quantitative), in both phantom and clinical imaging. For that purpose, image quality parameters such as noise, signal-to-noise ratio (SNR), contrast, contrast-to-noise ratio (CNR), contrast recovery coefficient (CRC) and also the quantification in terms of standardized uptake value (SUV) will be performed.

This dissertation is composed by five chapters. **Chapter I** concerns to the introduction of this thesis, including a brief context of PET, the relevance of the theme and description of the thesis organization. **Chapter II** refers to the background and support of the project. Physical principles of PET, performance of PET equipment, data acquisition and reconstruction, TOF, PET radiopharmaceuticals, CT, PET/CT and quantification of molecular imaging are some of the concepts covered in this chapter. **Chapter III** includes the objectives of the study, used materials and methods developed on this experimental research. **Chapter IV** contains the results and respective discussion plus the conclusion of the work. At last, final considerations and future perspectives are presented in **Chapter V**.

Chapter II – Background

2. Positron Emission Tomography (PET)

Nuclear medicine is a medical specialty that makes it possible to visualize and quantify biological processes (4). PET is an area of nuclear medicine and it concerns to an imaging technique of biochemical and functional biological processes at the cellular and molecular level with interest in several pathologies, particularly on cancer. Molecular imaging is different from traditional imaging because biomarkers are used to reach a specific target or pathways (5).

This imaging technique is only possible by detecting the radioactivity that is injected. The injected substances are usually called radiopharmaceuticals and consist in specific molecules, with affinity for a particular organ or tissue, labelled to positron (β^+ particle) emitting radionuclides.

2.1. Physical principles

An atom is electrically neutral when the number of negatively charged particles orbiting the nucleus (electrons) is the same as the number of positively charged particles in the nucleus (protons) (6). When an electron is withdrawn from or added to an atom, the latter is transformed into an ion, in other words a negatively or positively charged atom (6). The cohesion of an atomic nucleus results from the nuclear forces between protons and neutrons (6) (7). However, as the number of protons (Z, atomic number) gets larger, stable nucleus will have more neutrons than protons and, eventually, the nucleus becomes unstable (7). Therefore, the phenomenon of radioactivity is associated with the transformation of a nucleus by decay into a stable form (6) (7). The unstable nucleus decay by emitting a particle, as alfa or beta, or by emitting gamma rays (7).

The radionuclides used in PET decay by positron emission. As β^+ particles travel through human tissue, they give up their kinetic energy mainly by Coulomb[1] interactions with electrons. Once the rest mass of the positron is the same as that of the electron, the β^+ may undergo deviations in direction with each Coulomb interaction, giving up their kinetic energy after following a path through the tissue (8). Shortly after their emission, positrons give up their kinetic energy and annihilate with electrons in the body, producing two 511 keV gamma (γ) photons that are emitted with an angle of 180º apart (Figure 1). Detectors measure these γ-photons, their position and the time of their detection (coincidence detection) (4) (8) (9) (10). When two γ-photons are detected in coincidence, they trace a path between detectors called line of response (LOR) and it is recorded as a count in the system (4).

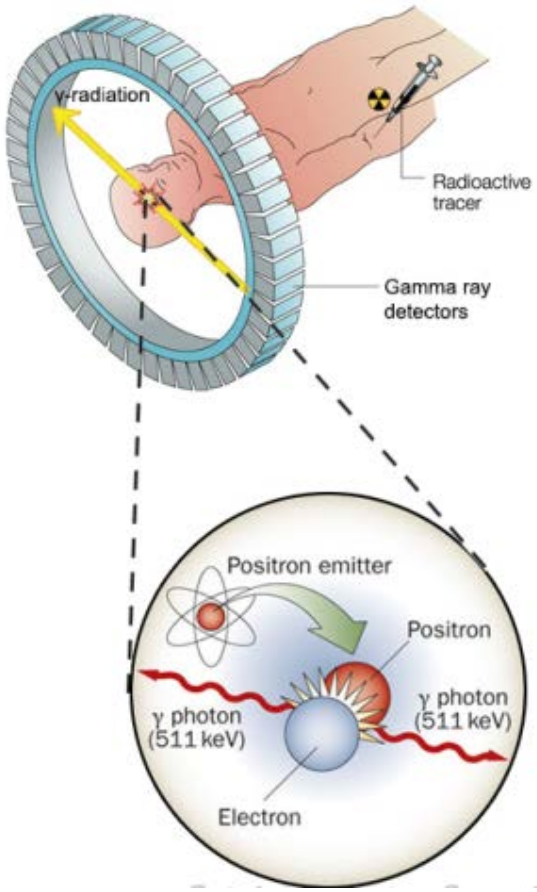

Figure 1. Detection illustration of γ-rays in a PET equipment. Adapted from **(10)**.

There are different types of coincidence events: true events, single-photon detection events, random coincidence and scattered coincidence (Figure 2). True coincidence events arise from pairs of photons that were produced from the same electron-positron annihilation and escape the body without undergoing further interactions; single-photon detection events

[1] SI unit of electric charge

can also arise when one of the two photons is attenuated within the patient; random coincidences arise from different annihilation event and introduce spurious counts along lines that do not necessarily pass through β^+-emitting sources (reduce image contrast); scattered coincidence events arise when one (or both) annihilation photons undergo Compton scattering interactions and do not pass through the site of annihilation event (degrade contrast and quantitative accuracy) (9) (11). There is another coincidence event – multiple detections – that can occur when three or more photons are detected at the same time, but these are usually discarded (5).

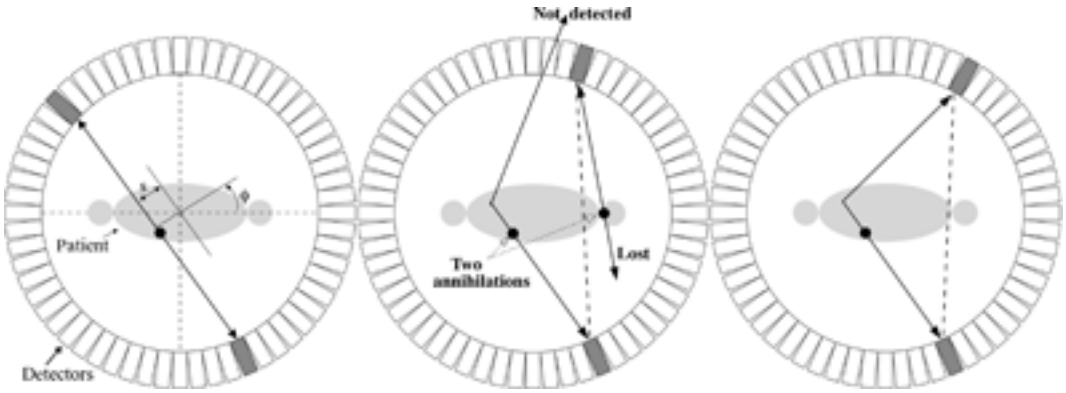

Figure 2. Transaxial view of detectors ring and patient demonstrating the types of coincident events. True coincidence (left), random (accidental) coincidence (centre) and scattered coincidence (right). The annihilations marked with solid black dots do not occur along the detected line-of-response in the second two cases leading to increased systemic noise in the data. Adapted from **(11)**.

2.1.1. Interaction of radiation with matter

The two most important general types of radiation emitted during radioactive decay are charged particles (as α and β particles) and electromagnetic radiation (as γ photons and x rays). These types of radiation transfer their energy to matter as they pass through it, which in this case is the human body. The principle mechanisms of interaction between the charged particles and the matter are, essentially, ionization and excitation of atoms and molecules (12).

High-energy photons transfer their energy to matter in complex interactions with atoms, nuclei and electrons. These interactions do not cause ionization directly, as do the charged-particle interactions. Nevertheless, some of the photon interactions result in the ejection of orbital electrons from atoms or in the creation of positive-negative electron pairs. These

electrons cause ionization effects, which are the basis for mechanisms by which high energy photons are detected and by which they cause radiobiological effects (12).

There are many possible interactions between photons and matter, such as photoelectric effect, Compton scattering, pair production, Rayleigh scattering and also Thomson scattering. Nonetheless, only two are significant to nuclear medicine: photoelectric effect and Compton scattering (12). In the practice of nuclear medicine, where gamma rays with energies between 50 keV and 550 keV are used, Compton scattering is the dominant type of interaction in materials with lower atomic numbers, such as human tissue (Z = 7.5).

The photoelectric effect is an atomic absorption process in which an atom absorbs totally the energy of an incident photon (12). The photon disappears and the energy absorbed is used to eject an orbital electron from the atom (photoelectron) (12) (Figure 3) (13). The photoelectric effect creates a vacancy in an orbital electron shell, leading to the emission of characteristic x rays or Auger electrons (12). The kinetic energy imparted to the photoelectron is deposited near the site of the photoelectric interaction by the ionization and excitation interactions of high energy electrons (12). The probability of photoelectric absorption increases rapidly with increasing atomic number of the absorber atom and decreases rapidly with increasing photon energy (8).

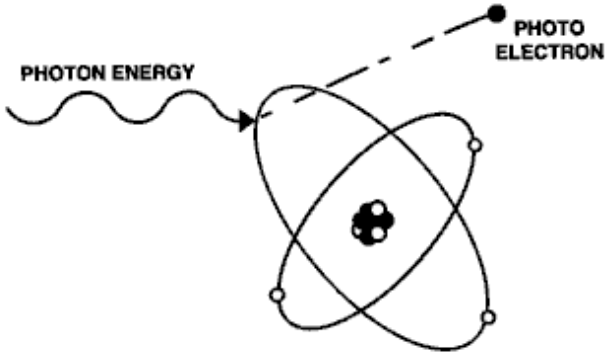

Figure 3. Scheme of photoelectric effect. Adapted from **(13)**.

In Compton scattering, a photon collides with a loosely bound outer shell orbital electron of an atom and the incident photon energy greatly exceeds the binding energy of the electron to the atom (8) (12). In the process the kinetic energy of the electron is increased and the photon is deflected through a scattering angle, changing its direction (8) (12) (Figure 4) (13). The energy transferred does not depend on the density, atomic number or any other property of the absorbing material; it is strictly a photon-electron interaction (12).

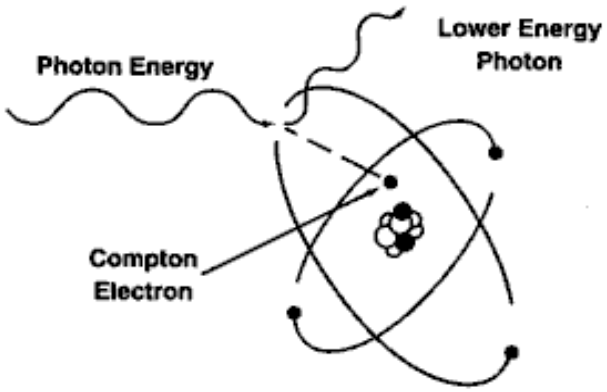

Figure 4. Scheme of Compton scattering. Adapted from **(13)**.

The two effects we have just described give rise to both absorption and scattering of the radiation beam.

2.1.2. Radiation detection

There are three major types of radiation detectors: gas-filled detectors, semiconductor detectors and scintillation detectors. Gas-filled detectors include ionization chambers, proportional counters and Geiger-Müller counters. Semiconductor detectors are essentially solid-state analogues of gas-filled ionization chambers and they are usually poor electrical conductors. The most common semiconductor detector materials used are silicon (Si), germanium (Ge) and more recently, cadmium telluride (CdTe) or cadmium zinc telluride (CZT) (12).

Scintillators are materials in which energy is released as visible light and can be of two different types: inorganic substances in the form of solid crystals or organic substances dissolved in liquid solution (12). Interaction of radiation with solid scintillation detectors is the basis of radiation detection in PET technology (14). In scintillation detectors, the amount of light produced is proportional to the energy deposited by the incident radiation in the scintillator (12). Although many scintillators detectors have been investigated, only a few have been used in PET (14). The choice of a detector is based on several characteristics: stopping power of the detector for 511 keV photons, scintillation decay time, light output per keV of photon energy and energy resolution of the detector (14). The detection efficiency of a detector is another important property in PET technology (14). Most of the scanners are equipped with new and fast detectors using new scintillation crystals (5). These materials contribute to a better count rate as they show a faster scintillation rise and decay time (5). A

shorter coincidence time window also can be applied, resulting in a decrease of random and scatter coincidences (5).

2.2. Performance of PET equipment

PET scanners share a common design, consisting in a stationary ring of scintillation detectors coupled with an array of photomultiplier tubes (PMTs). Detectors convert γ-photons into optical light, while PMTs convert this optical light to an electrical signal (9). The signal is then amplified, sorted by a pulse height analyser (PHA) and registered as a count (14).

Several parameters associated with the scanner are critical to good quality image formation, which include dead time, sensitivity, spatial resolution, energy resolution and timing resolution.

2.2.1. Dead time

Dead time is related with the amount and/or concentration of radioactivity that is underestimated at high counting rates. A detector requires a minimum time to distinguish two events as separated. Thus, when the system is not able to record an event after another event, this period of time is called dead time. PET scanners use empirical dead time models in which the observed count rate as a function of radioactivity concentration is measured for a range of object sizes and at different energy thresholds. Some systems apply a global dead time correction factor, whereas others apply corrections to individual pairs of detector modules. Some of the situations in which the corrections can be applied are first-pass cardiac studies, imaging studies near the bladder (due to the high levels of excreted radioactivity) and studies with very short-lived radionuclides (12).

2.2.2. Sensitivity

Sensitivity is defined as the number of counts per unit time detected by the device for each unit of activity present in a source (14). The sensitivity of PET detectors, as other imaging devices detectors, is determined mainly by the absorption efficiency of the detector

system and its solid angle of coverage of the imaged object (12). It depends on the geometric efficiency, detection efficiency, PHA window settings and the dead time of the system (14). Moreover, detection efficiency of a detector depends on the scintillation decay time, density, atomic number and thickness of the detector material (14). The geometric efficiency of a PET scanner is defined by the solid angle projected by the source of activity at the detector and it depends on the distance between the source and the detector, the diameter of the ring and the number of detector in the ring (14). The sensitivity of a scanner is highest at the centre of the axial field of view (FOV), decreasing toward the periphery, and increase with the number of rings (14).

2.2.3. Spatial resolution

Spatial resolution is defined as the minimum distance between two points in an image that can be detected by a scanner (14). It is a measure of the ability of the equipment to reproduce the image of an object, through the distribution of radioactivity in it (14). This parameter in PET imaging is affected by many factors such as positron range, detector size, annihilation photon non-collinearity, Compton scattering, off-axis detector penetration and patient motions during examination (15). Spatial resolution is estimated by the full-width at half-maximum (FWHM) of the line spread function (positron count distribution) obtained from measurement of activity distribution from a point source (14).

2.2.4. Energy resolution

The energy resolution of the scanner is related with the ratio of energy variance and fluctuations in the energy measurement. It is the ability of the detector to accurately determine the energy of the incoming radiation and is expressed as a percent of the energy of the incoming photons. Energy resolution also allows to distinguish against PET Compton scattered photons and lost energy before being measured. The energy resolution depends on the light output and the intrinsic energy resolution of the crystal. The light output is the number of scintillation photons produced by each incident photon ant it should be the highest possible, allowing the best spatial resolution and energy resolution (16).

The energy resolution is measured as the ratio of the FWHM of the full energy peak and the energy value at the full energy peak maximum. If a large proportion of the incident

photons register in the full-energy peak and the energy resolution of the detector system is good, then it is possible to discriminate against events arising from photons scattered within the object by rejecting those with a low measured energy.

2.2.5. Timing resolution

The timing resolution is characterized by the FWHM of the response to a given time interval event. The statistical fluctuation of the time interval between the arrival photon at the sensor and output pulse leading edge is defined as the timing resolution (17). Time resolution is a key parameter in the performance of a Time-of-Flight (TOF) PET scanner, and it is usually measured in the system with unscattered data and used as the width of the TOF kernel in reconstruction (18) (19).

The main limitation on timing resolution is the scintillator crystal, but newer crystals (such as LYSO) have more desirable qualities (shorter scintillation decay time, light output and energy resolution) (4). Ideally, it was expected that timing spectrum had a uniform distribution with a width equal to the system timing resolution (Δt), but in practice it has a Gaussian distribution with noise spread (18) (19).

2.3. Data acquisition and reconstruction

PET data are acquired directly into sinograms in a manner similar to matrix mode in planar imaging (20).

The process of calculating the 3D activity biodistribution from the measured sinograms including correction for random, scatter, attenuation, normalisation and dead time is called image reconstruction (5).

2.3.1. Acquisition mode

Before nowadays, PET/CT scanners were equipped with a physical collimator (septa) constituted by lead or tungsten ringed shields positioned within the FOV. Currently, PET uses a 3D imaging acquisition mode – electronic collimation (Figure 5). Due to LOR join the

two relevant detectors, positional information is gained from the detected radiation without the need for a physical collimator (5).

The main goal of septa (2D mode) was to reduce the contribution of random coincidences, scattered photons and photons that come from activity outside the FOV by shielding the detectors. When a physical collimator is used, directional information is gained by preventing photons which are uninteresting to the collimator face from reach the detector (5). In electronic collimation, these photons may be detected and used as signal. 3D acquisition mode has two major advantages: improved sensitivity (higher detection) and improved uniformity of the point source response function. On the other hand, it also increases random and scatter contributions, although new scintillation crystals help to decrease this flaw (5) (21).

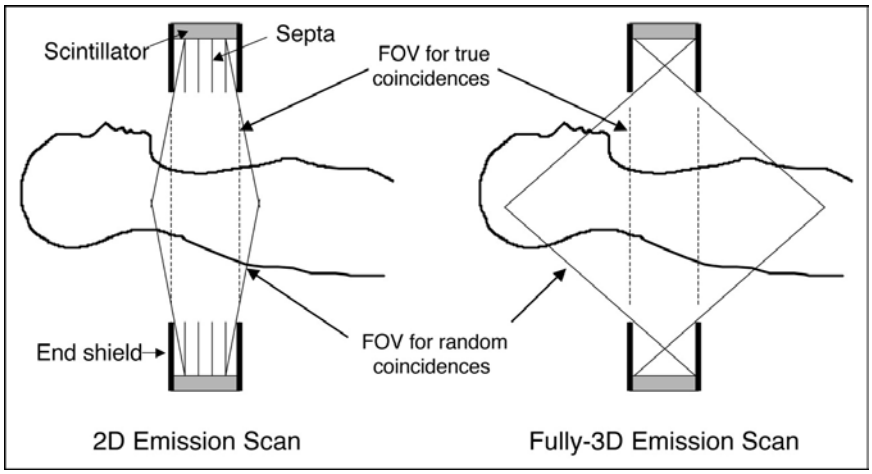

Figure 5. 2D acquisition mode (left) and 3D acquisition mode (right). Adapted from **(21)**.

2.3.2. Data organization

Each LOR corresponds to a particular pixel in the sinogram depending on its orientation angle and distance from the centre of the gantry (20). Sinograms contain the coincidences and the projections over all angles of the radioactivity distribution in the patient (5). For each coincidence detection, the corresponding LOR is determined, the pixel in the sinogram associated is located and the value in each pixel represents the number of coincidence detections between the detector pair (20). For each slice, a separate sinogram is acquired (20).

In the sinogram, the values along a horizontal row represent detections acquired along parallel LORs at the corresponding angle and each pixel value along the row is the sum of all

of the events acquired along the corresponding LOR. A collection of LOR sums is referred to as a projection, so each row in the sinogram is the projection of that slice along the angle (20).

More angular samples mean more rows in the sinogram and consequently more data to be stored. In some cases, the number of angular samples can be reduced without adversely affecting the reconstructed image quality. In order to reduce the number of angular samples, one would add every other row in the sinogram to the previous row and assume the resultant data were acquired half way between the 2 samples. In other words, LORs nearby are summed in a single medium LOR. This manner of reducing the angular sampling is referred to as *sinogram mashing*. Thus, the resultant raw data would only take up half as much disk space (20).

In 2D mode the acquired data are organized in a series of parallel slices that can be reconstructed independently, whereas in 3D mode PET must be rebinned to resemble 2D data before reconstruction or a 3D reconstruction algorithm has to be applied. The raw data from 2D PET can be organized in either sinograms (one for each slice) or in projections views (one for each projection angle) (20).

2.3.3. Reconstruction algorithms

Mathematical algorithms are used to reconstruct images of selected planes within the object from projection data (12).

Image reconstruction algorithms can be classified into analytical and iterative methods.

2.3.3.1. Analytical reconstruction

The most used analytical image reconstruction method is filtered back-projection (FBP) (5). In this method, the projection data is first backprojected (1D Fourier transform[2]), then filtered in Fourier space (with a ramp filter) and finally inverse Fourier transformed (2D Fourier transform) to obtain the filtered projection (22). This process has to be done to each projection angle.

FBP is a popular method due to the combination of accuracy, speed of computation and simplicity of implementation (22). It is a linear and a quantitatively robust method, although it

[2] The Fourier transform decomposes a signal into frequencies

is sensitive to noise and reconstructed images may contain streak artefacts (5). The ramp filter amplifies high frequency components, which are dominated by noise, leading to very noise reconstructions (22). This can be controlled by using a low-pass filter that reduces amplitude at high frequencies (22).

Analytical methods are preferred to reconstruct dynamic PET studies, once these studies consist of many frames with short scan times and thus poor statistics (iterative reconstruction may show biases/quantitative inaccuracies) (5).

2.3.3.2. Iterative reconstruction

The development of efficient algorithms has permitted widespread clinical use of iterative image reconstruction methods (22). Methods of iterative reconstruction have been developed to allow for more consistent compensation for physical effects and imaging system limitations (23).

In iterative reconstruction an image is generated by repeatedly estimating an image and its corresponding sinogram (5). Firstly is made an initial estimate of the object activity distribution and then the estimated projection is calculated by forward projecting the initial estimate (22). Based on the comparison between estimated and measured projections, the initial estimate is adjusted according to certain criterion (22). Iterations are continued until there is an optimal match between the estimated and the measured sinogram (5).

The disadvantage of these methods is that quantitative accuracy and SNR depend on the number of iterations (5). Too many iterations amplify noise to unacceptable levels and a few iterations result in quantitative inaccuracy (no convergence) (5). Convergence[3] depends on the underlying source distribution and optimal reconstruction settings may thus be different for different types of PET study (5).

Iterative reconstruction algorithms have been developed such as maximum likelihood expectation-maximization (MLEM) (22). This algorithm has consistent and predictable convergence behaviour, although it presents two main drawbacks: noisy images and slow convergence (22). To reduce the noise, a smoothing filter can be applied to the reconstructed image, in order to suppress high frequencies (22). To address the issue of slow convergence, different methods have been proposed to accelerate MLEM (22). The ordered subset expectation maximisation (OSEM) algorithm partitions the projection data into subsets and uses only one subset of data for each update, leading to significant acceleration compared with MLEM (22). One drawback of OSEM is that it is not guaranteed to converge

[3] The image reaching the *true* activity distribution

to maximum likelihood (ML) solution (22). Nevertheless, OSEM is currently the most widely use iterative reconstruction method (5) (22). For oncological whole-body studies (in comparison to FBP), OSEM reconstruction provides images with better image quality (5). The row-action maximization-likelihood (RAMLA) algorithm, related to the OSEM algorithm, has been implemented for direct reconstruction of 3D PET data, which eliminates 2D re-binning of the 3D data and employs partially overlapping, spherically symmetric volume elements called *blobs* in place of voxels (24) (25).

There are other iterative methods, such as algebraic reconstruction techniques (ART) and maximum *a posteriori* (MAP). ART reconstruction pretends to find an image that satisfies a set of known constraints that are determined by the PET data. The main limitation of ART is that it does not model the statistics of PET data, leading to complications in the presence of statistical noise. MAP seeks to maximize the posterior probability density instead of maximizing the likelihood function, so that an *a priori* model if the image distribution is enforced in the reconstruction. This method is about a smoothness constraint, which enforces a more elegant noise control method (22).

2.4. Time-of-Flight (TOF)

TOF PET systems are able to distinguish the arrival time of each photon, overcoming many problems associate to image reconstruction (4). TOF is used to localize the emission point along a LOR (18), with a certain degree of error based on the detection timing resolution (26), by measuring the difference in coincident photon detection times (4). This technique has been developed since 1960s, although it was used in clinic only in 1980s (18) (19), due to limited technologies (4). The need to improve signal-to-noise ratio (SNR) and to reduce random coincidences drove to the development of TOF PET scanners (18). Better detectors and electronics have been improved since then (18) (4) (19).

To generate 3D images in PET, coincident LORs are normally detected and recorded at many angles, and tomographic images are generated through traditional filtered back-projection or iterative reconstruction. In a TOF PET system, for each annihilation event the difference in arrival times between the two coincident photons is also measured. Even imperfect timing information helps to improve the reconstruction because TOF information serves to localize the coincidence, which reduces the propagation of noise along the LOR.

The distance that a given event is projected along the LOR is defined by an uncertainty Δx that can be much smaller (with good timing resolution) than the distance D (diameter of the

patient) over which counts would be distributed equally in the forward- and back-projection steps of non-TOF reconstruction. A reduction of noise can be equated to an increase in sensitivity, and this effective sensitivity gain was estimated at the center of a uniform distribution to be proportional to $D/\Delta t$ (Equation 1):

$$\Delta x = c \cdot \frac{\Delta t}{2} \qquad \text{(Eq. 1)}$$

where *c* is the speed of light, and *Δt* is the timing resolution (19).

2.4.1. TOF *versus* non-TOF systems

The non-TOF PET systems use lutetium oxyorthosilicate (LSO) and sodium iodide doped with thallium (NaI(Tl)) scintillators, while some TOF PET systems use barium fluoride (BaF_2) scintillators with a timing resolution of 450-750 ps. LSO PET systems show a timing resolution of 1.2 ns, whereas lutetium-yttrium oxyorthosilicate (LYSO)-based TOF PET systems have a timing resolution of 450-500 ps. Nevertheless, a commercial whole-body PET/CT scanner with a 309 ps timing resolution has already been developed. The gain due to TOF PET increases with an object size increase or with timing resolution improvement (18). Timing resolution is measured as the FWHM of the histogram of TOF measurements from a point source (timing spectrum) (18) (19). The main limitation on timing resolution is the scintillator crystal, but newer crystals (such as LYSO) have more desirable qualities (shorter scintillation decay time, light output and energy resolution) (4).

During reconstruction, with non-TOF PET systems, every voxel in an LOR is incremented by the same amount, while TOF PET relates the annihilation with timing resolution making a Gaussian distribution of the “most likely position” of annihilation (Figure 6) (26).

The conventional PET image quality degrades noticeably for large patients due to increased attenuation, leading to increase of scattered or absorbed photons, loss of true counts and increase of background (19). Another problem associated is the volume of distributed counts: larger body size means lower radioactivity concentration in an area or more amount of injected radioactivity (26). TOF can lead to bigger gains in image quality, especially for large patients, as it provides a gain in image SNR and reduces random coincidences. Improvements of TOF PET could be characterized as making a large body look like a small body (26).

TOF contributes to improve the trade-off between lesion contrast, image noise and total imaging time or injected activity, leading to more accurate and precise lesion uptake measurements and better lesions detection (18) (19) (Figure 6) (27). Furthermore, images with fewer counts may still have satisfactory image quality and TOF reconstruction improves structural details. Consequently, TOF can be beneficial in situations as dynamic imaging, respiratory gating and imaging with non-pure positron-emitters (e.g. Iodine-124) (19).

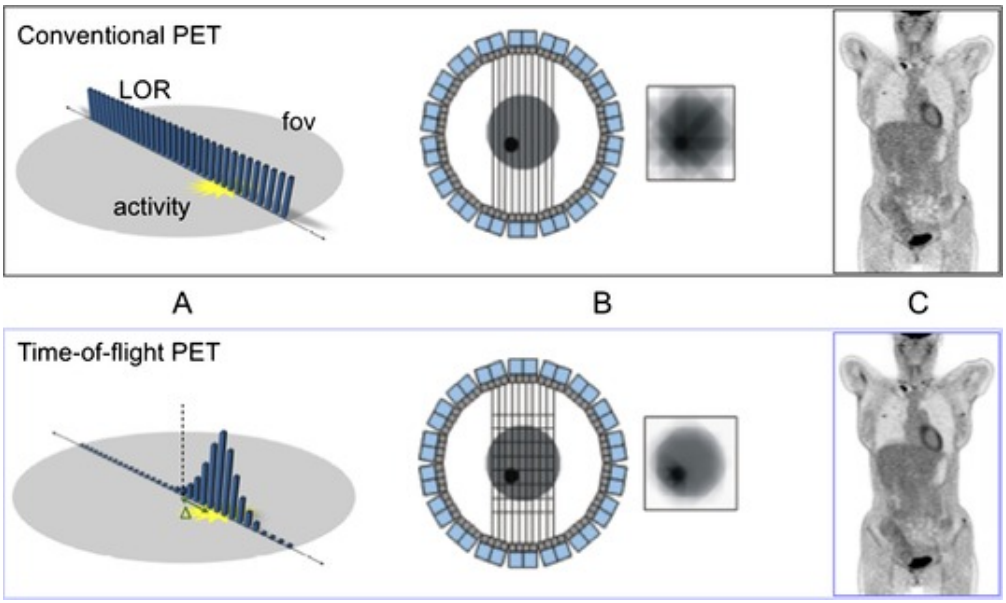

Figure 6. Conventional PET *vs* TOF PET. Adapted from **(27)**.

TOF information is also useful to overcome some CT artefacts as patient motion and truncation of the attenuation map that will affect attenuation correction and scatter estimate. Another great benefit is related to the area of limited-angle reconstruction, due to the PET detectors geometry (18).

Surti *et al.* (2015) observed that the lesion uptake and contrast converged more quickly and required less iterations to achieve the maximal contrast with TOF imaging than with non-TOF imaging. All lesions were visible after 2 minutes with TOF imaging, while with non-TOF imaging smaller lesions (10 mm) were still not visible after 5 minutes of scan (18).

2.4.2. Limitations and challenges of the TOF PET image

Currently, assessment of the exact location, within a couple of millimetres, with TOF is not practicable. The actual TOF technology provides a positional accuracy within about 10 cm FWHM (5).

The benefits of improved TOF PET imaging performance in the clinic have been used principally to reduce patient imaging acquisition times or to improve image quality in heavy patients. Improved image quality with TOF PET might be useful in some routine clinical situations as respiratory gating with a reduce penalty of image noise (due to a loss of counts) and monitoring disease progression or assessing tumour response to therapy (18).

Immuno-PET is growing area that uses long-lived β^+-emitting radioisotopes to track the localization of monoclonal antibodies. These applications perform imaging at a few days after injection of small doses of radiopharmaceutical and TOF PET can provide accurate with moderate imaging times (18).

The development of new scintillators that improve on the performance of systems can lead to further improvements in the system timing resolution. As an example, lanthanum bromide ($LaBr_3$), with a timing resolution of 375 ps, has a lower detection efficiency than LSO or LYSO, but high light output, which leads to improved timing and energy resolution. Furthermore, with the current introduction of PET combined with Magnetic Resonance Imaging (PET/MRI), new silicon PMTs had to be developed to operate within a magnetic field. These new PMTs provide fast timing performance and afford the only technologic solution to achieving TOF PET in PET/MRI equipment (18).

In the future, TOF PET may play an important role in situations that require low dose imaging and imaging with long-lived radioisotopes for target therapy (18).

2.5. PET radiopharmaceuticals

There are different radionuclides used in PET, such as fluorine-18 (^{18}F, half-life of 109.8 minutes), carbone-11 (^{11}C, half-life of 20.4 minutes), oxygen-15 (^{15}O, half-life of 2.04 minutes) and nitrogen-13 (^{13}N, half-life of 9.97 minutes), but the most common is the first one (4) (9).

The most used radiopharmaceutical in PET is ^{18}F-fluorodeoxyglucose (^{18}F-FDG), due to its appropriate characteristics (5) (9). The ^{18}F-FDG is an analogue of glucose labelled with ^{18}F that provides an early obtainment of metabolic information that is increased in cancerous cells (4) (28). ^{18}F-FDG is used not only for oncologic diagnosis and staging, but also in cardiology, neurology and infection imaging (4).

Another radioisotope with some similar physical properties to ^{18}F has been used for tumour imaging: Gallium-68 (^{68}Ga, half-life of 67.8 minutes). ^{68}Ga is an abundant short-lived positron emitter, with 89% positron branching, which subsequently decays to stable ^{68}Zn (29). This radionuclide eliminates the need of a near cyclotron (since it is produced in

generator), making an interesting alternative to ^{18}F. ^{68}Ga-DOTA-conjugated peptides can be useful for neuroendocrine tumour imaging (with somatostatin receptors) (30). Apart from DOTA-peptides, ^{68}Ga has been used to label various other peptides, bombesin being the most important. Bombesin receptors are overexpressed in prostate and breast cancer. ^{68}Ga-citrate shares a similar uptake pathway to conventional ^{67}Ga-citrate, making it promising tracer for infection/inflammation. ^{68}Ga-DOTA peptides seem to be the most promising owing to their practical advantages (easy synthesis process and potentially lower costs) and higher sensitivity for the detection of well-differentiated lesions (29). ^{68}Ga-Prostate Specific Membrane Antigen (^{68}Ga-PSMA) is a radiopharmaceutical that has also been used to study prostate cancer (31).

Some of other PET radiopharmaceuticals used in clinic are shown in Table 1 (9) (32) (33) (34).

Table 1. Radiopharmaceuticals used in PET and their applications.

Radiopharmaceuticals	Applications
^{18}F-FDG	Oncology, cardiology, neurology and infection imaging
^{18}F-FDOPA	Diagnosis of Parkinson's disease (decarboxylation and storage of dopamine); neuroendocrine tumour imaging
^{18}F-FMISO	Hypoxia imaging
^{18}F-florbetapir	Diagnosis of Alzheimer's disease (beta-amyloid plaques imaging)
^{11}C-PiB	Diagnosis of Alzheimer's disease (beta-amyloid plaques imaging)
^{11}C-acetate	Prostate cancer imaging
^{11}C-choline	Prostate cancer imaging
^{11}C-methionine	Brain tumour imaging
^{11}C-methylphenidate	Dopamine transporter
^{11}C-raclopride	D2 receptor density
^{15}O-H_2O	Blood flow; tissue perfusion
^{15}O-carbon monoxide	Blood volume
^{13}N-ammonia	Cardiac blood flow
^{68}Ga-DOTA-peptides	Neuroendocrine tumour imaging
^{68}Ga-PSMA	Prostate cancer imaging

3. Computed Tomography (CT)

Computed Tomography (CT) is a radiologic and anatomical technique that provides a diagnostic tool for a wide range of clinical indications, being also used as a complement for other imaging modalities. A CT system produces cross-sectional (slice) images of selected regions of the body, which can be used for different diagnostic and therapeutic purposes (35).

CT scanning was invented by Geoffrey Hounsfield in the 1970s (5). Shortly after the appearance of single-slice spiral CT scanners (early 1990s), CT performance has improved rapidly with the advent of multidetector arrays (36). Dual 4-slice CT scanners became available (1998), followed by 16-slice scanners (2002) and 64-slice scanners (2004) (36). Due to the increasing number of detector rows, faster rotation times have been accomplished (3 rotations per second) (36).

In CT imaging, the images of body tissues and organs represent the X-ray attenuation properties of the different tissues, in other words, the x-ray photons (coming from the X-ray tube) are attenuated in the patient's tissues and organs. The X-ray detector area is constituted by a radiation-sensitive material (cadmium tungstate or gadolinium-oxide), which converts photons into visible light. This light interacts with a silicon photodiode and it is converted into an electrical signal. Later, the electrical signal is amplified and converted into a digital signal. The linear attenuation coefficients (μ) of the different tissues are computed and images are then reconstructed from all the attenuation measurements, through mathematical algorithms (35).

The interaction between the radiation and matter depends on the photons energy, thickness of matter and electron density (35). Dense tissues, like compact bone (+1000 HU[4]), attenuate more X-rays than less dense tissues, such as fat (-80 to -100 HU) (5) (35). These differences in attenuation will result in a final image with correspondent contrast variations (35).

[4] The Hounsfield unit (HU) scale is a linear transformation of the original linear attenuation coefficient measurement into one in which the radiodensity of distilled water at standard pressure and temperature (STP) is defined as zero Hounsfield units (HU), while the radiodensity of air at STP is defined as -1000 HU. In a voxel with average linear attenuation coefficient μ, the corresponding HU value is therefore given by: $HU = 1000 \times \frac{\mu - \mu_{water}}{\mu_{water} - \mu_{air}}$. Thus, a change of one HU represents a change of 0,1% of the attenuation coefficient of water since the attenuation coefficient of air is nearly zero.

4. PET/CT

Current commercial PET/CT scanner designs consist of a multislice spiral CT scanner in tandem with a PET scanner. Figure 7 shows a schematic diagram of a typical PET/CT scanner, where a CT scanner is in tandem with a PET scanner and shares the same bed. Separate CT and PET scanners are fit within a single gantry. The patient can go through the CT and PET scanners successively while the bed moves, without repositioning. The separation of the FOV of the two scanners is compensated by the movement of the bed, so that the acquired images are intrinsically coregistered, which is an advantage over software image fusion (36).

Traditional PET scanners usually rely on a lengthy transmission scan for attenuation correction (AC) (36). With the introduction of PET/CT, CT provides not only accurate anatomical detail, but also an attenuation map (linear attenuation coefficients) with good image quality, thus eliminating the need for the transmission scan and substantially reducing the scan time (36). For a whole-body scan, it can reduce the scan time by at least 40% (36). Moreover, it contributes to an enhanced lesion quantification, and relatively high special resolution and sensitivity (9). The fusion between these two techniques compared to isolated PET, presents several advantages, such as: localization of functional disorders more precisely, distinction between benign lesions and malignant lesions, minimization of patient's motion, decrease of acquisition time, efficient attenuation correction of PET images and increase practitioner's reliability to interpret PET and CT images (1).

The first hybrid anatomical-functional imaging system was a dual-head scintillation camera combined with a low-power X-ray tube and detectors (37). The first commercial PET/CT scanner came onto the market in 2001 (36). Since then, it has been rapidly adopted by nuclear medicine and radiology departments (36). As a result, the sales of PET/CT scanners have drastically increased and in 2006 it completely replaced the sales of PET-only scanners (36).

The combination of PET and CT provides more information for clinicians and leads to more accurate diagnosis. It has been shown that PET/CT significantly improves diagnostic accuracy for a variety of cancers compared to PET or CT alone and sometimes can even lead to a treatment change (36).

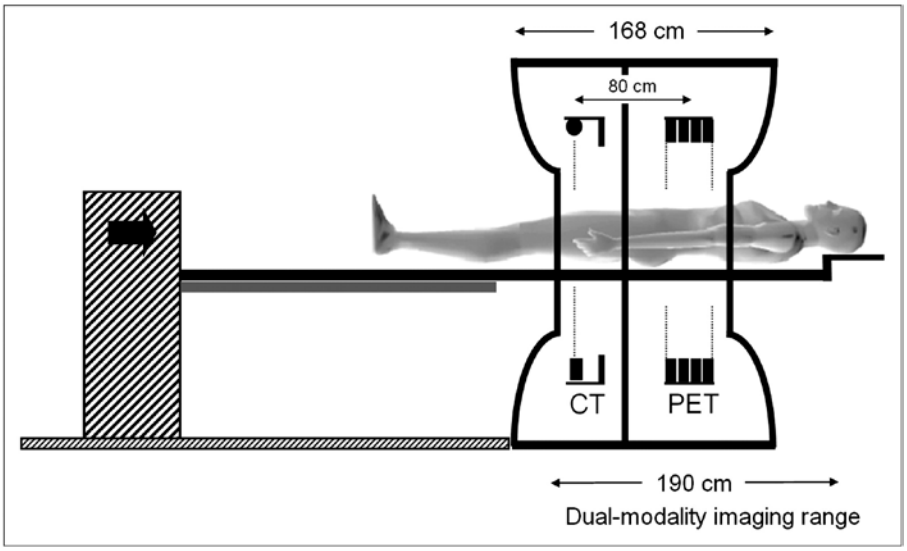

Figure 7. Schematic of early PET/CT scanner design. Adapted from (36).

4.1. PET/CT imaging procedure

Following radiotracer injection and uptake, the patient is positioned and a low-dose CT scout scan (topogram) performed (2 to 10 seconds) (38) (35). The topogram is used as an anatomical reference for the subsequent scans (35). The regions to be scanned are also defined in this step (35). Right after that, acquisition planning is performed on the topogram, the CT spiral is acquired and reconstruction begins (30 seconds to 2 minutes) (38) (35). The CT scan is usually performed at 100-140 kV[5] (35). The images are then scaled voxel by voxel to 511 keV by applying the bilinear scaling function (36). The advantage of bilinear scaling is that it requires only a simple threshold and avoids a complex segmentation of the CT images (36). While CT reconstruction completes, the patient is automatically positioned for the PET scans and images are acquired (38). After CT reconstruction, the PET attenuation correction factors (ACF) are computed (38). An attenuation map is constructed, in which anatomical density differences in the patient's body structures are used to correct the absorption of the annihilation photons (35). Thereupon, each PET bed position is reconstructed as its data become available (38). Assembly of the whole-body image is completed 60 seconds following the last acquisition (38). Finally, PET/CT fused images are reviewed (38). A schematic diagram of a standard PET/CT protocol can be observed in Figure 8.

[5] Penetrating power of X-ray

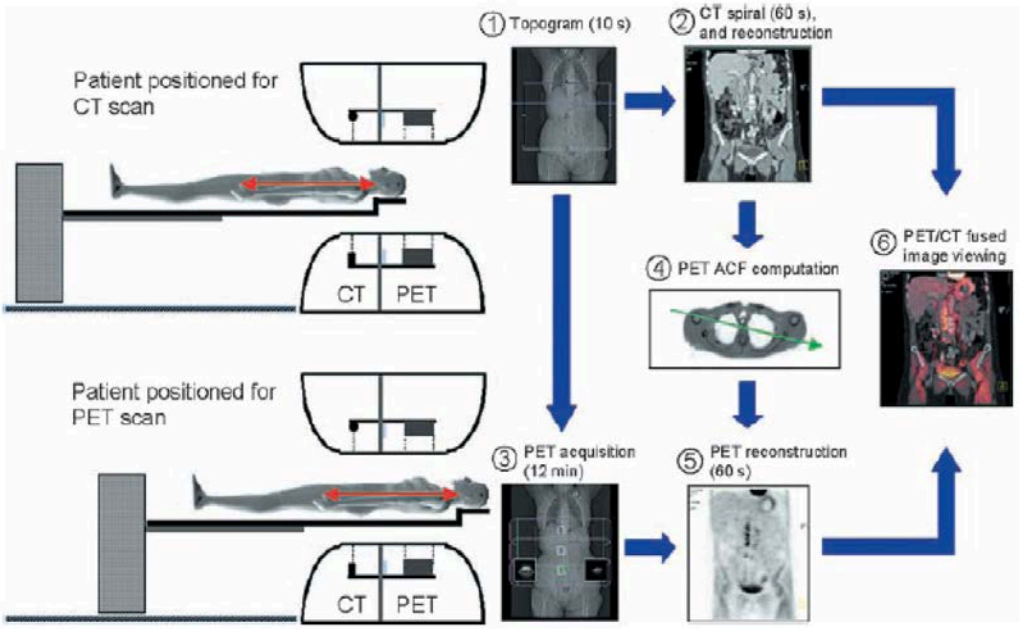

Figure 8. Standard PET/CT protocol. A topogram is acquired (1). Patients undergo the CT (2) and PET acquisitions (3). After attenuation correction (4), PET images are reconstructed (5) and fused images are obtained (6). Adapted from **(38)**.

5. Quantification of molecular imaging

Nuclear medicine is based on the differential uptake of a radiopharmaceutical in normal and abnormal tissue to determine the structural or functional status of the patient. Lesion detectability reflects the ability to detect low-contrast signals in noisy background and is related to image quality (39).

Detection in PET images strongly depends on the ability to recognize the signal pattern in the presence of noisy background that in turn, is limited by the capability of the imaging system to detect objects with very low contrast relatively to the background level and to spatially resolve a focal uptake.

The image quality of reconstructed PET data can be evaluated using the several parameters described below.

5.1. Image quality parameters

Noise, signal-to-noise ratio (SNR), contrast, contrast-to-noise ratio (CNR) and contrast recovery coefficient (CRC) are generally mentioned as measures of image quality.

Noise in images can be random or structured. Random noise is caused by random statistical variations in counting rate (39) (12) and it is calculated as (Equation 2):

$$random noise = \sigma = \sqrt{N} \quad \text{(Eq. 2)}$$

where σ is the standard deviation (SD) and N corresponds to the number of photons in target. Structured noise refers to non-random variations in counting rate and interferes with the perception of the structures of interest (e.g. radionuclide distribution itself or caused by system artefacts) (Equation 3) (39) (12):

$$structured noise = \frac{\sigma}{N} \quad \text{(Eq. 3)}$$

Low-pass filtering (smoothing) can be used in an effort to improve noisy images, although there should be a compromise between filters, in order to maintain the image quality (40). In

reconstruction, noise spreads over voxels along the LOR and it is defined as *Δx*. The effective sensitivity gain at the centre of a uniform cylinder (phantom) due to TOF information is given by $D/\Delta x$, wherein *D* is the object size (18) (19). Noise in reconstructed images (errors in the measurement) (26) can be calculated as the average pixel-to-pixel percent SD in the regions of interest (ROIs) or the background variability measure prescribed by National Electrical Manufacturers Association (NEMA).

SNR is a term used to represent the ratio between a signal (meaningful information) and the background noise. In practice, this ratio divides the mean number ($\bar{x}$) of detected photons (counts) in a ROI by the SD of the signal (σ) (Equation 4):

$$SNR = \frac{signal}{noise} = \frac{\bar{x}}{\sigma} \quad \text{(Eq. 4)}$$

Higher SNR means that image is less noisy image (15). By increasing the contrast (through improved spatial resolution) or decreasing noise (through increased sensitivity), SNR can be increased.

Contrast refers to the differences in image intensity between areas of the imaged object containing different concentration of radioactivity (39). This parameter is calculated by subtracting the count rate over a normal tissue (B) from the count rate over a lesion (T) and dividing the result by the count rate over the lesion plus the count rate over a normal tissue (41), as shown below (Equation 5):

$$Contrast = \frac{T - B}{T + B} \quad \text{(Eq. 5)}$$

Only the contrast is not enough to qualify an image. CNR allows a better measure of the image quality (15) and it is related with detection of a lesion or other object in an image, distinguishing between lesion and noise (39) (12). A higher CNR value is necessary in order to differentiate between tissues and between healthy and pathological tissues (15). The greater the contrast between lesions and surrounding tissue, greater the signal (39). CNR is calculated by the next equation (Equation 6) (42):

$$CNR = \frac{T - B}{\sqrt{\sigma_T^2 + \sigma_B^2}} \quad \text{(Eq. 6)}$$

When there is no background signal, SNR and CNR are equivalent (39).

In general, the quality of an image can be described (quantitatively) by its SNR. The SNR directly affects diagnostic and quantitative accuracy. In essence, then, a major goal of nuclear medicine equipment is to maximize the SNR in an image. The CNR refers to the ability in PET to distinguish between various contrasts in an acquired image and the inherent noise in the image. The mean signal recovery of SNR and CNR were evaluated as a function of the lesion size and the lesion activity uptake.

CRC is a performance measure related with lesion uptake, which in TOF imaging converges more quickly to achieve the maximal contrast (18) and it is calculated as (Equation 7):

$$CRC = \frac{\left(\frac{C_{lesion}}{C_{background}} - 1\right)}{\left(\frac{A_{lesion}}{A_{background}} - 1\right)} \quad \text{(Eq. 7)}$$

where C_{lesion} and $C_{background}$ are the average counts in the sphere and background ROIs, respectively and $\frac{A_{lesion}}{A_{background}}$ is the ratio of the true activities in the sphere and background (19) (43).

Higher contrast values are often related with noisier images. In practice, this contrast is provided by the radiotracer's distribution. The goal of the imaging system is to preserve this contrast in the image. Contrast is maintained by avoiding blurring, which smears counts from higher activity regions into lower activity regions (and vice versa), thus reducing image contrast. In this way, spatial resolution and contrast are closely linked.

The volume recovery coefficient (VRC) of an object is the ratio of the apparent activity concentration to the true activity concentration and it is defined as (Equation 8):

$$VRC = \frac{V_{measured}}{V_{true}} \quad \text{(Eq. 8)}$$

where $V_{measured}$ is the measured lesion volume and V_{true} is the real lesion volume (42).

The Percentage Error (PE) measures the size of the error in percentage terms. It is about comparing a guess or estimate to an exact value, given by (Equation 9):

$$\%error = \frac{X_{measured} - X_{true}}{X_{true}} \times 100 \quad \text{(Eq. 9)}$$

where $X_{measured}$ corresponds to the image quality parameter that we want to compare with the image quality parameter obtained for to the default variable(s) used in clinical routine (X_{true}) (42).

5.2. Standardized Uptake Value (SUV)

PET imaging is by its very nature quantitative and the commonest quantitative measure quoted in PET/CT reports is the standardized uptake value (SUV). SUV is a semi-quantitative index to quantify glucose metabolism in FDG oncology studies (9). This parameter is defined as the ratio between the radiopharmaceutical concentration (expressed in kBq/mL) and the decay corrected injected activity normalized by a given factor (Equation 10) (44) (45):

$$SUV_{LBM} = \frac{Tissue\ activity\ concentratiom}{Injected\ activity \,/\, Patient\ mass} \quad \text{(Eq. 10)}$$

The tissue activity concentration is obtained from the PET image and it must be corrected for physical effects (as attenuation and scatter) and calibrated in appropriate units (decay corrected back to injection time). Patient lean body mass (lbm) is used in an effort to standardize data across patients with different body fat (9). Two other normalization factors can be used: body weight (SUV_{bw}, kg/mL) and body surface area (SUV_{bsa}, m^2/mL) (44).

SUV_{max} is related with the SUV of the maximum intensity voxel within a ROI and SUV_{peak} is defined as the average SUV within a small ROI. When using SUV_{max} or SUV_{peak}, the information of the tumour is reduced to the measurement within a limited region of the tumour. Nonetheless, there is another measure (SUV_{mean}) that reflects the whole tumour. In other words, it is the average measure of SUV within calculated boundaries of a tumour (44).

SUV can be affected with several factors, such as biological factors (uptake period, patient motion and breathing and blood glucose levels), technical factors (relative calibration between PET scanner and dose calibrator, residual activity in syringe, incorrect synchronisation of clocks, injection *vs* calibration time and quality of administration) and

physical/data analysis-related factors (scan acquisition parameters, image reconstruction parameters and use of contrast agents) (5). SUV is also susceptible to partial volume effect (PVE), what means that SUV calculated for small tumours is likely to underestimate the true value (9).

PVE can be caused by two distinct phenomena: the 3-dimensional (3D) image blurring introduced by the finite spatial resolution of the image system and the image sampling (46). Due to the finite spatial resolution, the image of a small source is a larger but dimmer source, in other words, the measured image is formed by the convolution of the actual source with 3D point spread function (PSF) of the imaging system (46). PVE can be also referred to the image sampling (46). In PET, the radiotracer distribution is sampled on a voxel grid (46). This means that pixels on edges of source include both source and background tissues (46). Consequently, signal intensity in these pixels is mean of signal intensities of underlying tissues (46). Part of signal emanating from source is seen outside actual object and therefore is described as spilling out (46). Likewise for any hot lesion of a small size and embedded in a colder background, PVE spreads out the signal[6] (46). PVE also affects the apparent tumour size (46). The fusion of the PET and CT images clearly shows this discrepancy between the tumour contours as displayed on the CT image and on the PET image (46). The biases introduced by PVE depend on several parameters, such as tumour size and shape, surrounding tissues, spatial resolution in reconstructed images, image sampling and measurement method (46). The magnitude of the PVE is also influenced by ROIs: large ROIs average out the signal from heterogeneous tumours; smaller ROIs than the size of the tumour can reflect the most metabolically active part (9).

[6] This effect typically occurs whenever the tumour size is less than three times the FWHM of the reconstructed image resolution.

Chapter III – Materials and methodology

6. Objectives

The main goal of this work is to determine the shortest acquisition time per bed of a TOF PET/CT system, without compromising the image quality of PET in what regards to quantitative assessment. It is intended to investigate the gain in image quality that can be achieved in a TOF scanner for different acquisition times per bed, using a NEMA phantom to simulate a human torso with hot (radioactive) and cold (non-radioactive) spheres.

As specific objectives, it is intended to:

- Analyse qualitative and quantitatively the CT-based attenuation correction (CTAC) images for different acquisition times;
- Calculate and analyse image quality parameters as noise, SNR, contrast, CNR, CRC and VRC and also the quantification in terms of SUV;
- Compare the measurements referred above for the images with different acquisition times;
- Compare the measurements obtained with the NEMA phantom and the clinic image (patient);
- Verify whether it is feasible to decrease the acquisition time to below 2 min per bed position without substantially reducing the detection rate and diagnostic image quality.

7. Materials

7.1. PET/CT Philips Gemini TF 16

Images were acquired with a hybrid system PET/CT of *Philips Medical Systems*: GEMINI TF 16, Figure 9 (47). This equipment has enhanced performance ant it consists in a 3D PET scanner with TOF functionality and a CT scanner – Brilliance model – of 16 slices, available at *Champalimaud Foundation*. The equipment has a LYSO scintillator integrated with a timing resolution of 575 ps, an energy resolution of 11.7% and a spatial resolution near the centre about 4.8 mm (in both the transverse and the axial directions). The sensibility (at the centre) is 7000 counts per second (cps)/MBq (NEMA) and above 14000 cps/MBq (TOF). It also has 420 PMTs incorporated and allows a 4D mode acquisition. The axial and transaxial FOV are 18 cm and 67.6 cm (maximum), respectively (1) (3).

Figure 9. PET/CT Philips Gemini TF 16 scanner. Adapted from **(47)**.

7.2. Germanium-68/Gallium-68 generator

The radionuclide used in the study is the ^{68}Ga, eluted from the Germanium-68/Gallium-68 (^{68}Ge/^{68}Ga) generator, for its favourable characteristics and availability. ^{68}Ga is an abundant short-lived (half-life 67.8 min) positron-emitter (β^+ max. energy 1.89 MeV; 2.9 mm mean range in water) (29). ^{68}Ga has similar physical characteristics to ^{18}F (half-life and radioactive decay) and eliminates the need of a near cyclotron, making an interesting alternative to ^{18}F.

High-quality and clinically useful PET images can be obtained using ^{68}Ga, while also imparting a lower radiation absorbed dose to patients (is rapidly excreted in the urine, greatly diminishing the potential radiation absorbed dose). The ability to free PET imaging from the previously inextricable and sometimes onerous capital equipment costs and complex organic chemistry associated with the cyclotron production of PET radionuclides is indeed very attractive. There are similarities between the current ^{99m}Tc Single-photon emission computed tomography (SPECT) paradigm and the ^{68}Ga PET. The rapid in-growth of ^{68}Ga on the generator allows for multiple elutions approximately every two hours (48).

^{68}Ge/^{68}Ga generator is used in nuclear medicine to produce the positron-emitting radionuclide ^{68}Ga. The parent isotope ^{68}Ge has a half-life of 270.95 days and can be easily delivered to hospitals. ^{68}Ga can be easily eluted from the generator any time at the place of the application and used for different purposes (49).

The ^{68}Ga generator of a chromatographic type is a glass column with a sorbent based on tin dioxide (SnO_2) or titanium dioxide (TiO_2). The parent radionuclide ^{68}Ge is fixed on this sorbent. The column is placed into the lead shielding container and provided with eluent and eluate lines. ^{68}Ga (in ionic +3 oxidation state), which is formed as a result of ^{68}Ge decay, is eluted as chloride using 0.1 M of hydrochloric acid (HCl) solution. Prepurification of the eluate is often employed to minimize ^{68}Ge breakthrough and to reduce the amount and volume of HCl in the solution (29) (49).

7.3. Torso NEMA phantom

NEMA/International Electrotechnical Commission (NEMA/IEC) body phantom were used to acquire images. The phantom is used to evaluate reconstructed image quality in whole body PET imaging and it consists on a torso phantom (18 cm length and 9.7 L of volume) with six hollow spheres (wall thickness ≤ 1 mm) of various inner diameters – 10, 13, 17, 22, 28 and 37 mm – to simulate cold and hot lesions and an additional cylindrical insert with 50

mm diameter placed in the centre of the phantom to simulate lung (43) (50), as illustrated by Figure 10 (51).

This phantom can be used for:

- Simulation of whole-body imaging using PET and camera-based coincidence imaging techniques;
- Evaluation of reconstructed image quality in whole-body PET and camera-based coincidence imaging;
- Determination of the coincidence count rate characteristics in brain and cardiac imaging;
- Evaluation of the relationship between true coincidence count rate and radioactivity;
- Determination of the address errors caused by address pile up;
- Evaluation of the count loss correction scheme (50).

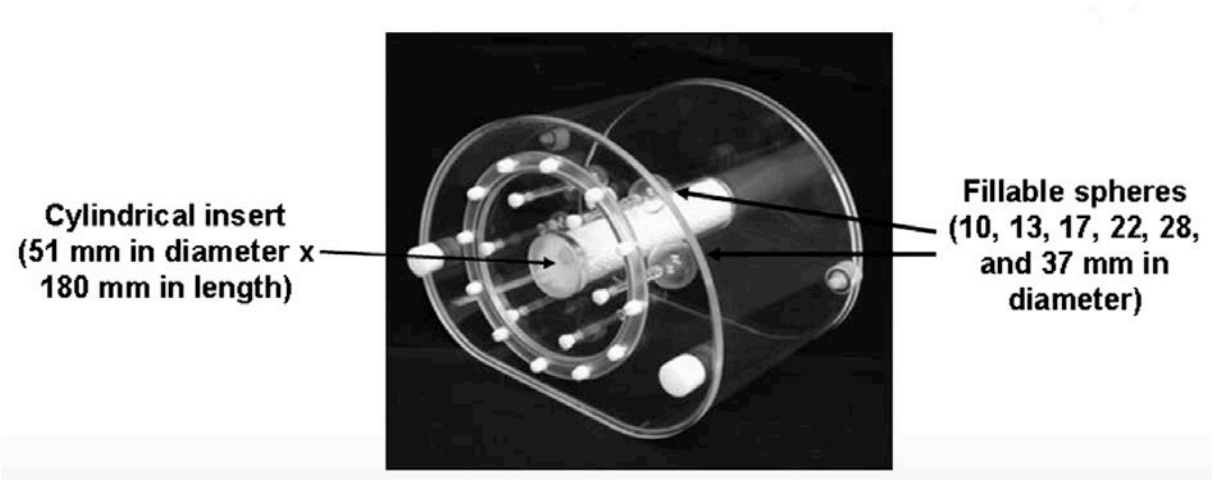

Figure 10. Phantom (NEMA IEC Body Phantom; Data Spectrum Corp.) with multiple fillable spheres and cylindric insert that can be filled with polystyrene to provide minimally attenuating material, simulating lung in otherwise uniform water-filled volume. Adapted from **(51)**.

7.4. Software resources

Image processing was reached with the Philips software. For qualitative and quantitative analysis, *Medical Image Data Examiner* (AMIDE) and Philips DICOM Viewer software were used. For statistical analysis, the Microsoft Office Excel was used.

8. Methodology

In order to develop this dissertation, it was performed a prospective study between January and April of 2016 at the Nuclear Medicine service of *Champalimaud Foundation*. It was collected a non-probabilistic convenience sample, including the images of a torso NEMA phantom with four hot spheres (10, 13, 17, 22 mm) for five different acquisition times: 30, 45, 60, 80 and 120 s. Also, it was collected a probabilistic sample, consisting of an aleatory patient.

To develop this experimental investigation, two phases were performed. Phase one was accomplished, using for the case a NEMA phantom, while phase two was done with a patient. In each phase, injection of ^{68}Ga, acquisition and data processing were achieved. Qualitative and quantitative analysis were performed with the software resources mentioned before.

8.1. Phase 1 – Phantom imaging

The ^{68}Ga was eluted from the ^{68}Ge/^{68}Ga generator with an activity of 417 MBq (per 4 mL). The background of the phantom was filled with ^{68}Ga at an activity concentration typical of what is seen in patient studies (370 MBq/70 kg or 5.3 kBq/mL) and the hot spheres were sequentially filled with activity concentration 8 times that the background, approximately (43). From the eluted activity, 51.5 MBq of ^{68}Ga was added to the NEMA phantom, for background, and it was filled with distilled water until the volume of the phantom, 9.7 L. In order to fill the spheres, a 10 mL syringe was prepared with 480 kBq of ^{68}Ga and a saline solution. Only the four smaller spheres were filled with radioactivity (hot spheres) – 116.75 kBq each (time of decay and residual activity on the syringe were considered). The two bigger spheres were filled with distilled water (nonradioactive water), as shown in Figure 11. The purpose of this measurement is to produce images simulating those obtained in a whole-body study with both hot and cold spheres of the NEMA phantom. The spheres were filled with a particular needle[7] (22 G, 20 cm), once the spheres are located in the middle of the phantom and so the radioactivity would be confined to them.

[7] The cold spheres were filled in first place, so that they would not be radioactively contaminated.

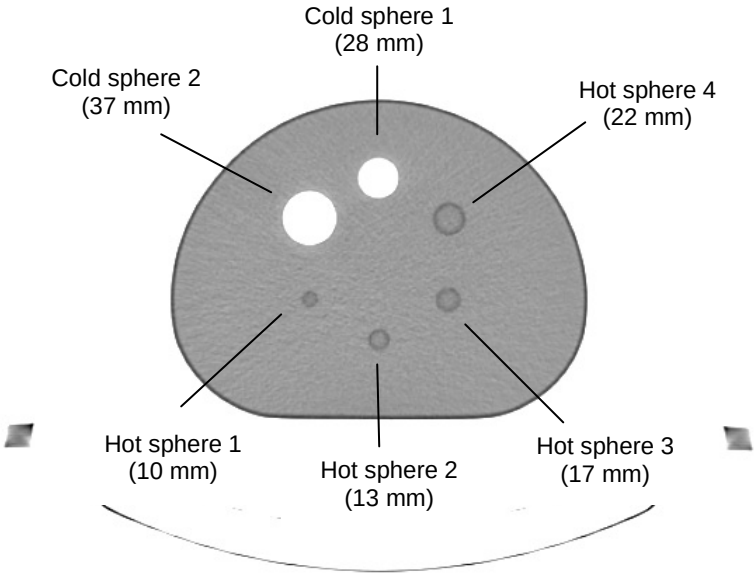

Figure 11. Scheme of hot and cold spheres of the NEMA phantom.

The acquisition was performed in the PET/CT Philips Gemini TF 16, illustrated by Figure 12. The operating parameters of the scanner had to be adjusted, as they would be for a typical patient study, including the radionuclide. For CT acquisition, it was used an electric potential of 140 kV and an electric current of 60 mA. Images were reconstructed using a 3D RAMLA algorithm, with the default parameters used in routine clinical whole body image reconstructions.

The tomographic images were acquired with 30, 45, 60, 80 and 120 seconds per bed position each. After the acquisition, the images were reconstructed with CTAC and processed in the Philips software. The data was analysed in both AMIDE and Philips DICOM Viewer and quantification of molecular imaging (reported in subchapters 5.1. and 5.2. of chapter II) and respective statistical analysis were performed in Microsoft Excel.

Figure 12. Acquisition studies with the NEMA phantom and the PET/CT Philips Gemini TF 16.

8.2. Phase 2 – Patient imaging

The radiopharmaceutical, ^{68}Ga-PSMA, was produced in the ^{68}Ge/^{68}Ga generator at a temperature between 105 and 110ºC. The elution of the peptide was made 10 minutes after start heating and the elution of the radioisotope was made after that (during 1 minute). Also, 1 mL of etanol 50% and 5 mL of sodium chloride (NaCl) 0.9% were added to the solution. Whenever it was inserted a solution in the generator, a syringe of air was injected to maintain the pressure inside the vials.

The patient (male with 64 years old), indicated to prostate adenocarcinoma staging, was submitted to a questionnaire about his clinical history (previous surgeries, medical exams and clinical analysis) and then he was injected with an activity of 112 MBq, based in his weight (81 kg).

The patient was positioned in supine with the arms above the head for acquisition at the tomograph. The operating parameters of the scanner were the same used for the phantom acquisition. Images of whole body were acquired at 30, 60 and 90 min after the radiotracer injection with 80 s per bed. Right after the 90 min images acquisition, three additional images were acquired with one bed and 30, 45 and 60 seconds each at a FOV in the upper abdominal including different tissues, as liver, spleen, heart, kidneys, bowels and vertebras. After the acquisition, the method of reconstruction, processing and analysis were the same as used for the phantom imaging, previous described in the subchapter 8.1 of chapter III.

Chapter IV – Results and discussion

9. Results

9.1. Image quality parameters

9.1.1. Phantom imaging

Image quality was compared for different sphere sizes of the NEMA phantom (10, 13, 17 and 22 mm, named ROI_1, ROI_2, ROI_3 and ROI_4, respectively) according to different acquisition times (30, 45, 60, 80 and 120 seconds). Figure 13 (same conditions, including slice number and contrast level) shows that as acquisition time increases, the image quality also increases. As time per bed increases, clearer are the spheres in the reconstructed images. Depending on the sphere size and the contrast level applied, it is possible to distinguish the sphere from the background. In this case, the contrast level applied for the five images is the same and all the four hot spheres can be noticed, although their distinctness is directly proportional to size and acquisition time. Spheres edges are more defined with longer acquisition times per bed.

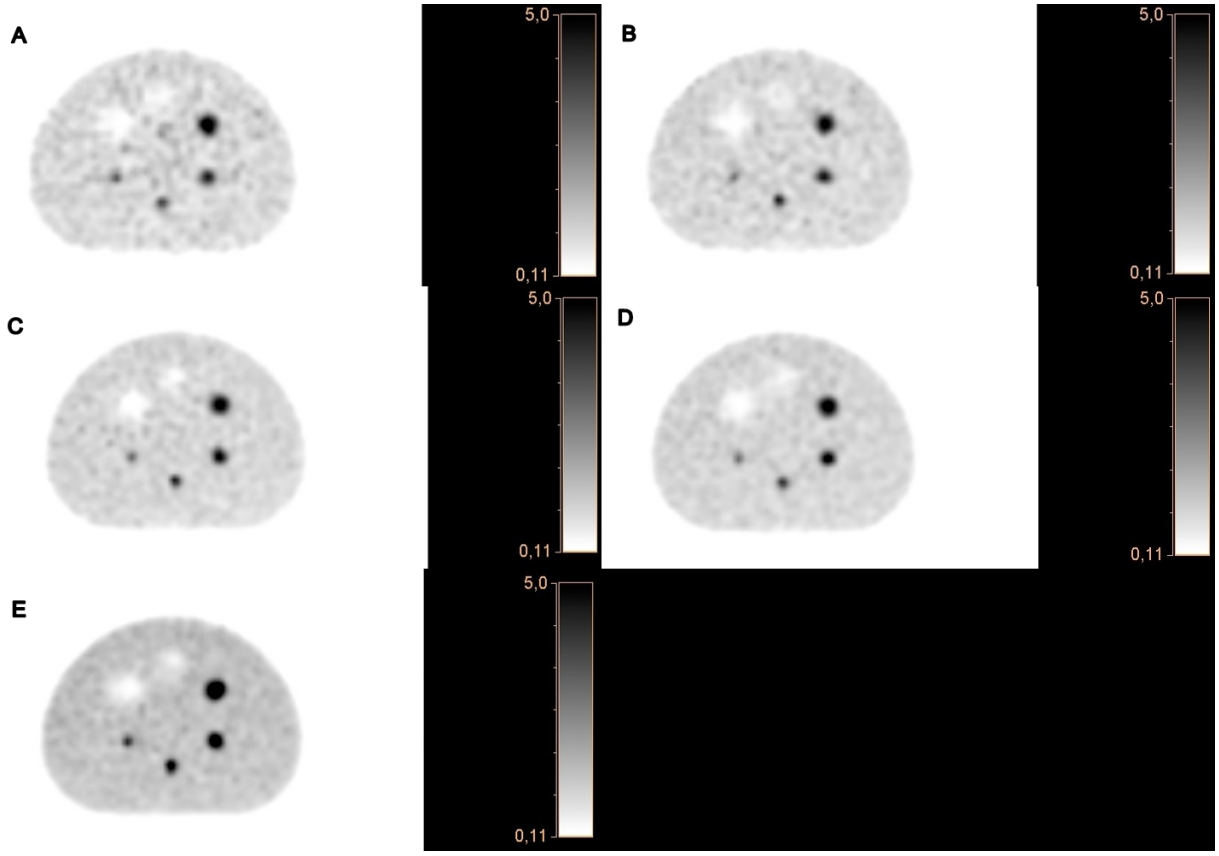

Figure 13. Transverse plane of the NEMA phantom (whole body CTAC) for 30 s (A), 45 s (B), 60 s (C), 80 s (D) and 120 s (E) acquisitions.

Image quantitative analysis was performed, considering the different sphere sizes and the different acquisition times per bed (mentioned before). Counting rate (mean counts) and standard deviation were collected and registered (Table 2). Real volumes (mm^3) and measured volumes (mm^3) of the spheres are shown in Table 3. Images quality parameters as noise, SNR, contrast, CNR, CRC and VRC were calculate and analysed (Table 4 to Table 8 and Figure 14 to Figure 19).

Table 2. Mean counting rate and standard deviation (σ) for the different ROIs (spheres sizes) and acquisition times.

Acquisition time (s)	Mean counting rate (counts)					σ (counts)				
	ROI_1	ROI_2	ROI_3	ROI_4	ROI_{bck*}	ROI_1	ROI_2	ROI_3	ROI_4	ROI_{bck*}
30	342	341	505	653	180	53	93	147	217	27
45	428	581	753	868	250	64	151	213	271	32
60	639	782	1157	1257	347	98	223	345	366	48
80	889	1002	1590	1687	411	109	235	525	541	44
120	1388	1592	2470	2589	677	203	398	773	798	50

* Background

Table 3. Real volume (V_{true}) and measured volume ($V_{measured}$) for the different ROIs and acquisition times.

Acquisition time (s)	V_{true} (mm^3)				$V_{measured}$ (mm^3)			
	ROI_1	ROI_2	ROI_3	ROI_4	ROI_1	ROI_2	ROI_3	ROI_4
30	520	1150	2570	5570	755	2310	3764	8379
45	520	1150	2570	5570	776	2352	3764	8479
60	520	1150	2570	5570	796	2310	3823	8580
80	520	1150	2570	5570	796	2310	3823	8580
120	520	1150	2570	5570	755	2310	3764	8379

Table 4. SNR values for the different ROIs and acquisition times.

Acquisition time (s)	SNR			
	ROI_1	ROI_2	ROI_3	ROI_4
30	6.45	3.67	3.44	3.01
45	6.69	3.85	3.54	3.20
60	6.52	3.51	3.35	3.43
80	8.16	4.26	3.03	3.12
120	6.84	4.00	3.20	3.24

Table 5. Contrast values for the different ROIs and acquisition times.

Acquisition time (s)	Contrast			
	ROI_1	ROI_2	ROI_3	ROI_4
30	0.31	0.31	0.47	0.57
45	0.26	0.40	0.50	0.55
60	0.30	0.39	0.54	0.57
80	0.37	0.42	0.59	0.61
120	0.34	0.40	0.57	0.59

Table 6. CNR values for the different ROIs and acquisition times.

Acquisition time (s)	CNR			
	ROI_1	ROI_2	ROI_3	ROI_4
30	2.72	1.66	2.17	2.16
45	2.49	2.14	2.34	2.26
60	2.68	1.91	2.33	2.47
80	4.07	2.47	2.24	2.35
120	3.40	2.28	2.31	2.39

Table 7. CRC values for the different ROIs and acquisition times.

Acquisition time (s)	CRC			
	ROI_1	ROI_2	ROI_3	ROI_4
30	0.12	0.12	0.25	0.36
45	0.10	0.18	0.27	0.34
60	0.11	0.17	0.32	0.36
80	0.16	0.20	0.39	0.42
120	0.14	0.18	0.36	0.38

Table 8. VRC values for the different ROIs and acquisition times.

Acquisition time (s)	VRC			
	ROI_1	ROI_2	ROI_3	ROI_4
30	1.45	2.01	1.46	1.50
45	1.49	2.05	1.46	1.52
60	1.53	2.01	1.49	1.54
80	1.53	2.01	1.49	1.54
120	1.45	2.01	1.46	1.50

The graphic illustrated by Figure 14 shows the SNR with time increase for the four hot spheres of the NEMA phantom. The smallest sphere (ROI_1) was the one with better signal-to-noise ratio, particularly for 80 seconds (SNR = 8.16), followed by the second smallest sphere (ROI_2) (SNR between 3.51 and 4.26). The two larger hot spheres (ROI_3 and ROI_4) show constant lower and similar SNR (higher SNR for ROI_3 is 3.54 at 45 seconds and for ROI_4 is 3.43 at 60 seconds).

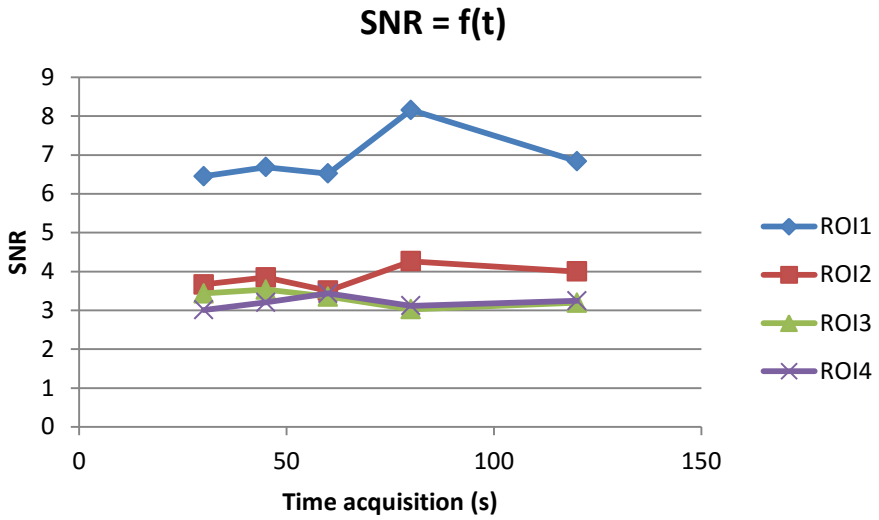

Figure 14. SNR for the different ROIs, as a function of the acquisition time.

Both noise (Figure 15) and contrast (Figure 16) tend to grow with time acquisition increase and these image quality parameters are higher for ROI_4, followed by ROI_3, ROI_2 and ROI_1, respectively.

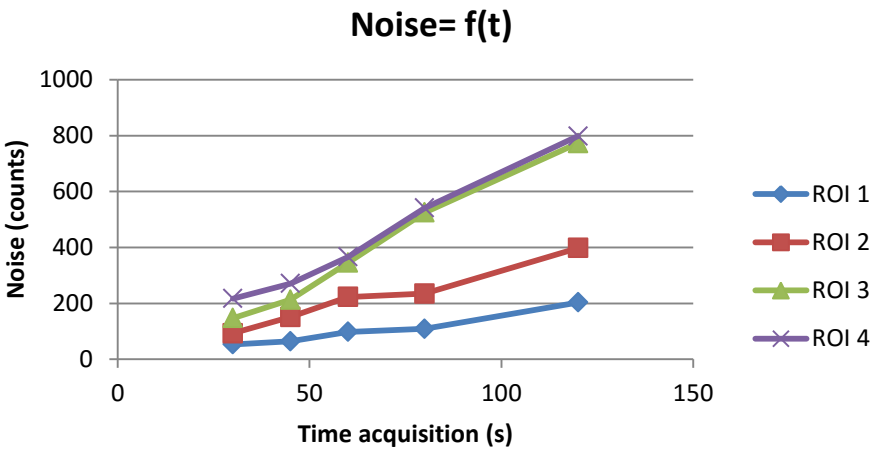

Figure 15. Noise for the different ROIs as a function of the acquisition time.

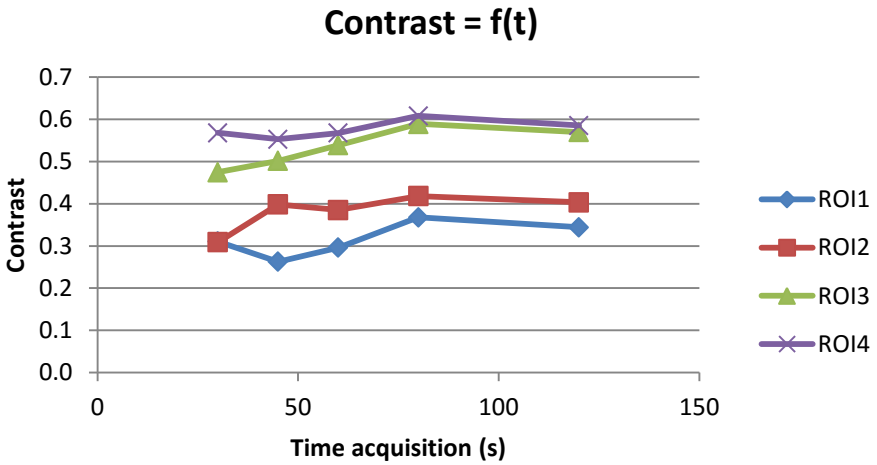

Figure 16. Contrast for the different ROIs as a function of the acquisition time.

The results for the CNR, Figure 17, show that this parameter is higher for ROI_1, especially at 80 seconds of acquisition time (CNR = 4.07). The curves of ROI_3 and ROI_4 appear to have a similar behaviour, while ROI_2 shows lower CNR for 30, 45 and 60 seconds (1.66, 2.14 and 1.91, respectively), higher CNR for 80 seconds (2.47) and similar CNR to ROI_3 and ROI_4 for 120 seconds (ROI_2 = 2.28, ROI_3 = 2.31 and ROI_4 =2.39).

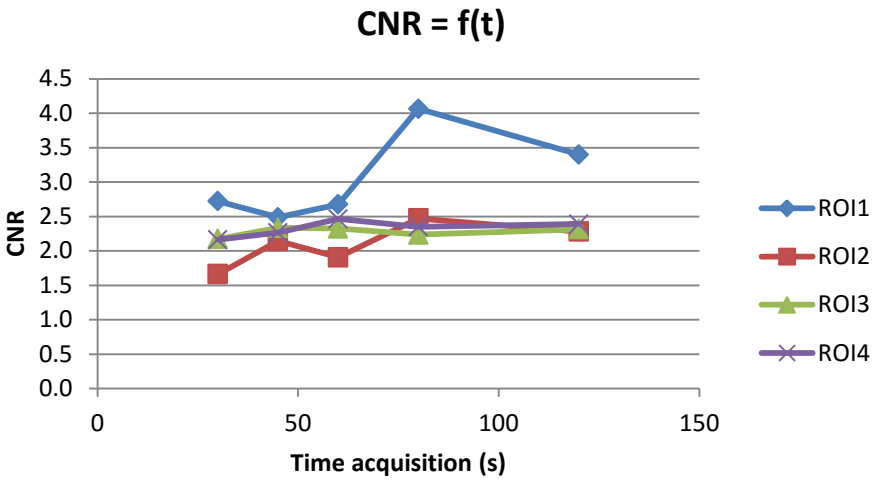

Figure 17. CNR for the different ROIs as a function of the acquisition time.

Analysing Figure 18, the four spheres have higher CRC for 80 seconds and ROI_4 ensures higher values, followed by ROI_3, ROI_2 and ROI_1, respectively. In general, the curves tend to grow with time increase.

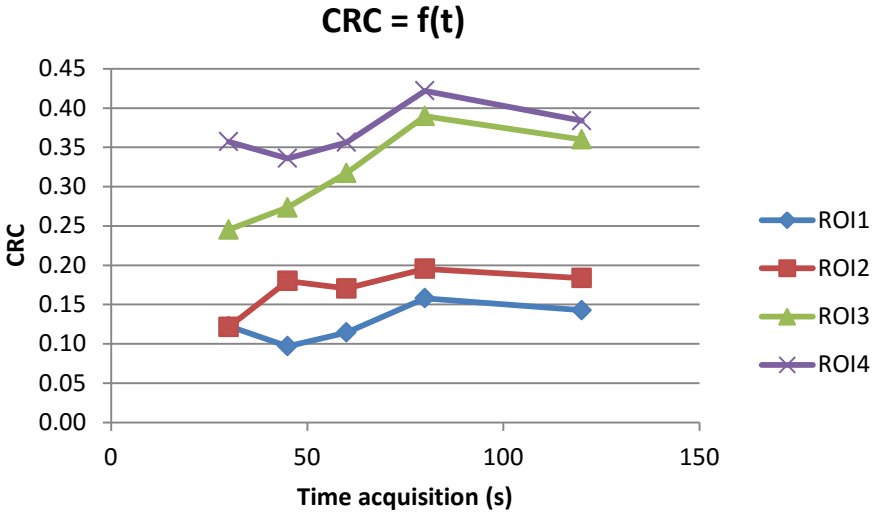

Figure 18. CRC for the different ROIs as a function of the acquisition time.

VRC is constant with time increase for the four spheres, although it is higher in ROI_2 (2.0) (Figure 19).

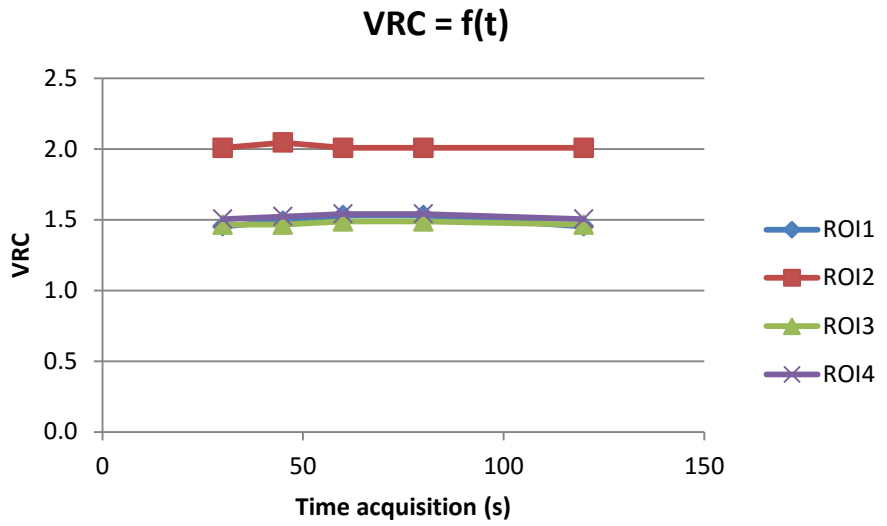

Figure 19. VRC for the different ROIs as a function of the acquisition time.

The standard errors measurements between the different acquisition times and the acquisition time per bed position commonly used in clinical PET/CT scanners at the Nuclear Medicine service of *Champalimaud Foundation* (80 s) for the parameters of image quality are shown in Table 9. The percentage errors were ≤ 21% for SNR, ≤ 29% for contrast and ≤ 39% for both CNR and CRC.

Table 9. PE values between the different acquisition times for the parameters of image quality.

		30 *vs* 80 s	**45 *vs* 80 s**	**60 *vs* 80 s**	**120 *vs* 80 s**
SNR	ROI_1	21 %	18 %	20 %	16 %
	ROI_2	14 %	10 %	18 %	6 %
	ROI_3	13 %	17 %	11 %	6 %
	ROI_4	3 %	3 %	10 %	4 %
Contrast	ROI_1	16 %	29 %	19 %	6 %
	ROI_2	26 %	5 %	8 %	4 %
	ROI_3	19 %	15 %	9 %	3 %
	ROI_4	7 %	9 %	7 %	4 %
CNR	ROI_1	33 %	39 %	34 %	16 %
	ROI_2	33 %	13 %	23 %	8 %
	ROI_3	3 %	4 %	4 %	3 %
	ROI_4	8 %	4 %	5 %	2 %
CRC	ROI_1	23 %	39 %	28 %	11 %
	ROI_2	38 %	8 %	13 %	6 %
	ROI_3	37 %	30 %	19 %	8 %
	ROI_4	15 %	20 %	16 %	9 %

9.1.2. Patient imaging

Image quality was compared for different acquisition times (30, 45, 60 and 80 seconds)[8]. Figure 20 (same acquisition conditions) shows no significant differences between 30, 45 and 60 s. Organs are clearer for 80 s in the reconstructed images. Noise levels presented in patient images are much superior to the level of noise presented in the images of the phantom.

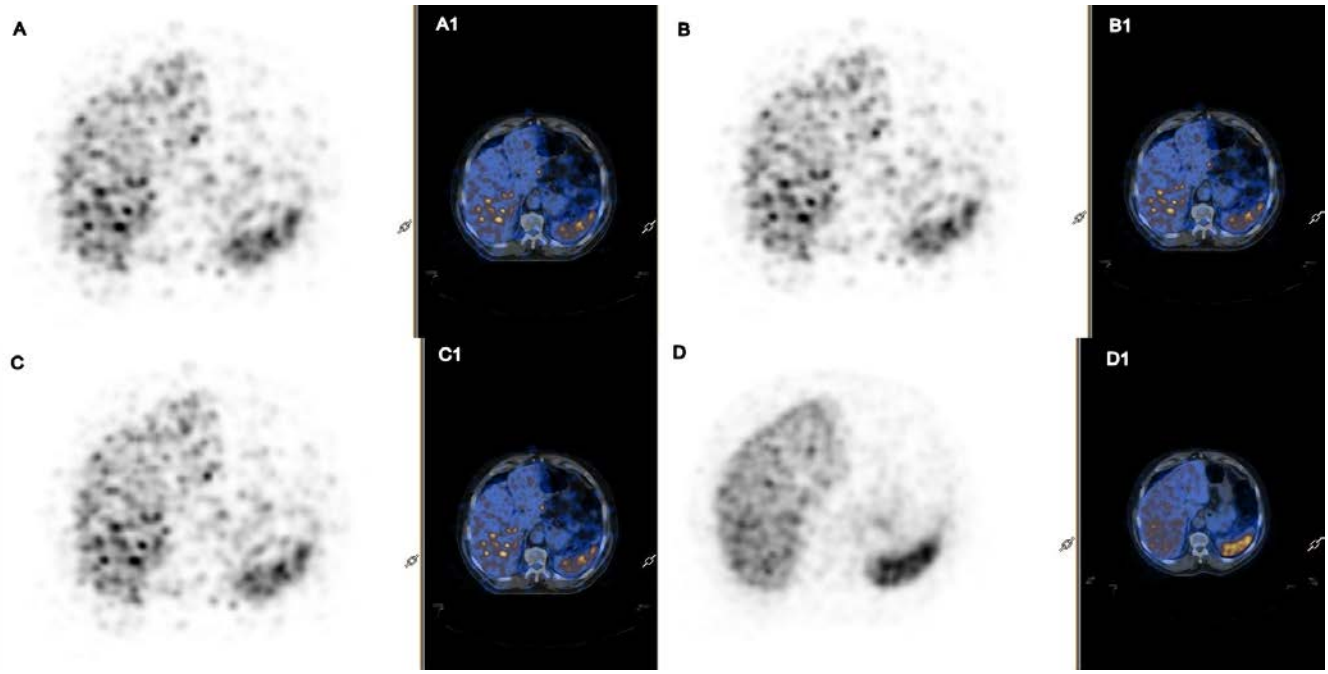

Figure 20. Transverse plane of patient imaging (whole body CTAC) for 30 s in PET (A) and PET/CT (A1), 45 s in PET (B) and PET/CT (B1), 60 s in PET (C) and PET/CT (C1) and 80 s in PET (D) and PET/CT (D1) acquisitions.

In order to extract the image data, three circular ROIs were delineated in each image: one for liver, one for spleen and another for background.

Image quantitative analysis was performed, considering the different acquisition times per bed position and three different tissues (liver, spleen and bone[9]). Counting rate (mean counts) and standard deviation, σ, were collected and registered (Table 10). Images quality parameters as noise, SNR, contrast and CNR were calculate and analysed (Table 11 and Figure 21 to Figure 24).

[8] Higher color intensity (black) represents upper tracer uptake.
[9] Normal bone marrow (in vertebrae) was considered as background, since it shows low tracer uptake and it has less than a quarter of the counts in liver and spleen.

Table 10. Mean counting rate and standard deviation (σ) for the different tissues and acquisition times.

Acquisition time (s)	Mean counting rate (counts)			σ (counts)		
	Liver	Spleen	Bone	Liver	Spleen	Bone
30	26	58	5	11	17	8
45	50	69	5	23	20	4
60	52	103	1	22	36	1
80	202	373	35	32	77	14

Table 11. SNR, contrast and CNR values for the different tissues and acquisition times.

Acquisition time (s)	SNR			Contrast		CNR	
	Liver	Spleen	Bone	Liver	Spleen	Liver	Spleen
30	2.36	3.41	0.63	0.68	0.84	1.54	2.82
45	2.17	3.45	1.25	0.82	0.86	1.93	3.14
60	2.36	2.86	1.00	0.96	0.98	2.32	2.83
80	6.31	4.84	2.50	0.70	0.83	4.78	4.32

The graphic illustrated by Figure 21 shows the SNR with time increase for the three tissues under study (liver, spleen and bone). Spleen shows a higher signal-to-noise ratio for all the acquisition times, except for 80 s (SNR_{liver} = 6.31; SNR_{spleen} = 4.84). Bone shows the lowest SNR for the different acquisition times (0.63 < SNR < 2.50). SNR is constant for 30, 45 and 60 s in the three tissues.

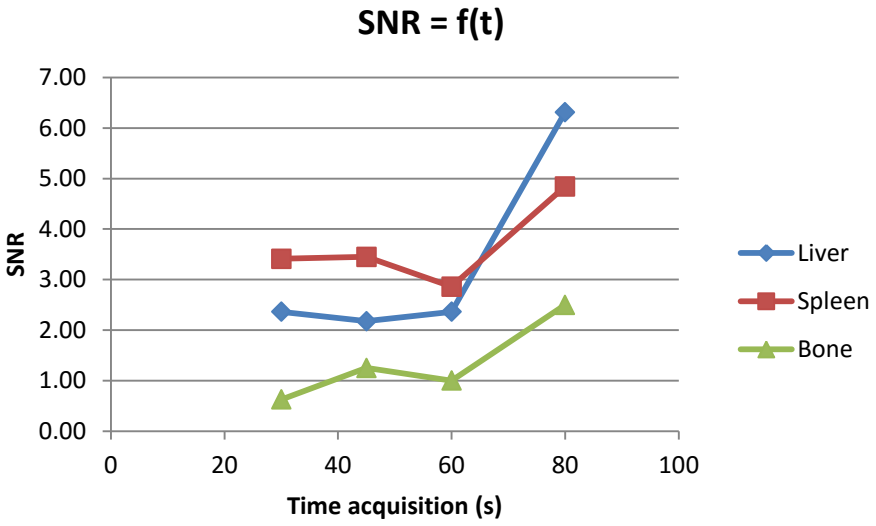

Figure 21. SNR for the different tissues, as a function of the acquisition time.

From the graphic illustrated by Figure 22, noise level grows in images with time acquisition increase, especially for 80 s. Generally, spleen shows a higher amount of noise and bone shows a lower amount of noise.

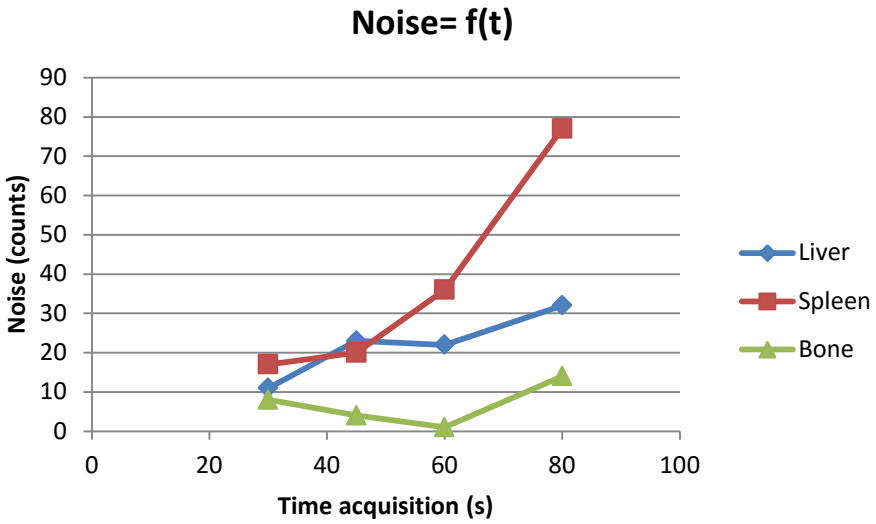

Figure 22. Noise for the different tissues, as a function of the acquisition time.

Both liver and spleen have a similar behaviour for contrast, as shown by Figure 23. Both tissues show a high contrast over the background (liver: contrast ≥ 0.68; spleen: contrast ≥ 0.83). For 80 s, contrast is lower in both cases.

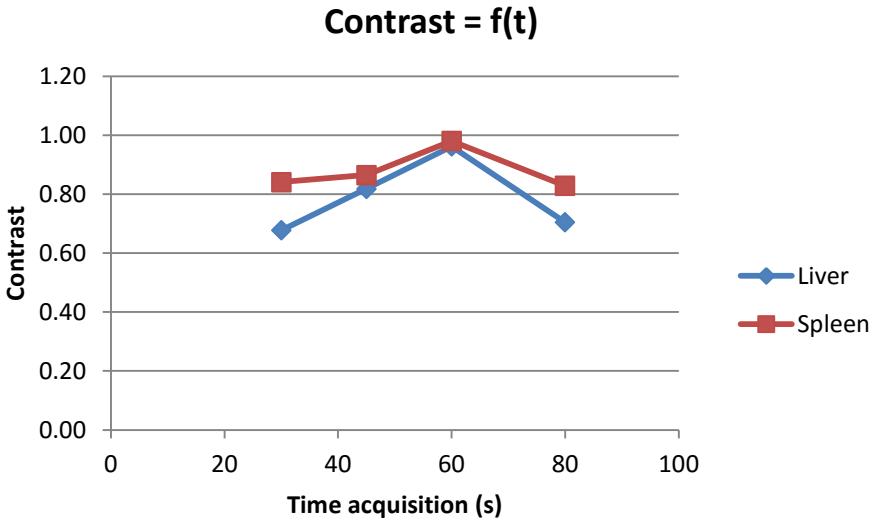

Figure 23. Contrast for the different tissues, as a function of the acquisition time.

The results for the CNR, Figure 24, show that this parameter is higher in spleen, except for 80 s (SNR_{liver} = 4.78; SNR_{spleen} = 4.32). The curves of liver and spleen grow with acquisition time increase.

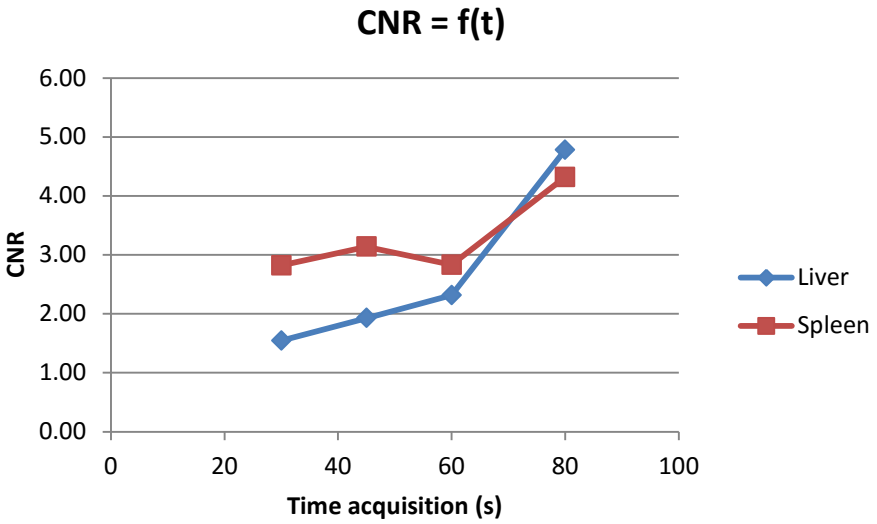

Figure 24. CNR for the different tissues, as a function of the acquisition time.

The standard errors measurements between the different acquisition times and the acquisition time per bed position commonly used in clinical PET/CT scanners at the Nuclear Medicine service of *Champalimaud Foundation* (80 s of acquisition time per bed position) for the parameters of image quality are shown in Table 12. In general, the percentages of the standard errors were inferior for contrast (≤ 37 %) and very high for SNR (≤ 75 %) and CNR (≤ 68%). Between the different tissues, spleen has a lower PE than liver for all the parameters of image quality. There are no significant differences between the acquisition times.

Table 12. PE values between the different acquisition times for the parameters of image quality.

		30 *vs* 80 s	**45 *vs* 80 s**	**60 *vs* 80 s**
SNR	Liver	63 %	66 %	63 %
	Spleen	30 %	29 %	41 %
	Bone	75 %	50 %	60 %
Contrast	Liver	4 %	16 %	37 %
	Spleen	2 %	4 %	18 %
CNR	Liver	68 %	60 %	52 %
	Spleen	35 %	27 %	34 %

9.2. SUV

9.2.1. Phantom imaging

Correlation of the SUV measurements between the different acquisition times per bed position was measured with the *Pearson* correlation coefficient. For that, we considered the time acquisition of 80 s as the "variable of control".

As mentioned in the subchapter 5.2., the SUV_{max} is the highest voxel value within a ROI, and is therefore independent of the size of the ROI, whereas the SUV average (SUV_{mean}) is the mean uptake value of all voxels within an ROI (and therefore is not ROI size independent). SUV_{max} values are typically used for abnormal lesions, whereas SUV_{mean} values are best used for organ based uptake assessment.

SUV_{max}, SUV_{mean} and standard deviation of SUVs are presented in Table 13. SUV_{max} is also shown in Figure 25.

Table 13. SUV values (mean and maximum) and correspondent standard deviation (σ_{SUV}) for the different ROIs as a function of the acquisition time.

Acquisition time (s)	SUV_{max}				SUV_{mean}				σ_{SUV}			
	ROI_1	ROI_2	ROI_3	ROI_4	ROI_1	ROI_2	ROI_3	ROI_4	ROI_1	ROI_2	ROI_3	ROI_4
30	2.5	2.9	4.7	6.0	1.9	1.9	2.8	3.7	0.3	0.5	0.8	1.2
45	2.1	3.5	4.4	5.3	1.6	2.2	2.8	3.3	0.2	0.6	0.8	1.0
60	2.3	3.5	5.3	5.5	1.8	2.2	3.3	3.5	0.3	0.6	1.0	1.0
80	2.4	3.2	5.8	5.8	1.9	2.1	3.4	3.6	0.2	0.5	1.1	1.1
120	3.4	4.6	8.0	7.7	2.6	3.0	4.7	4.9	0.4	0.8	1.5	1.5

Analysing Figure 25, SUV_{max} tend to increase with longer acquisition times and it is higher for ROI_4, except for 120 s (8.0 in ROI_3 and 7.7 for the ROI_4). ROI_3 has a similar behaviour to ROI_4 for 60, 80 and 120 seconds. ROI_1 shows the lowest SUV_{max} ($2.1 < SUV_{max} < 2.5$), followed by ROI_2 ($2.9 < SUV_{max} < 4.6$).

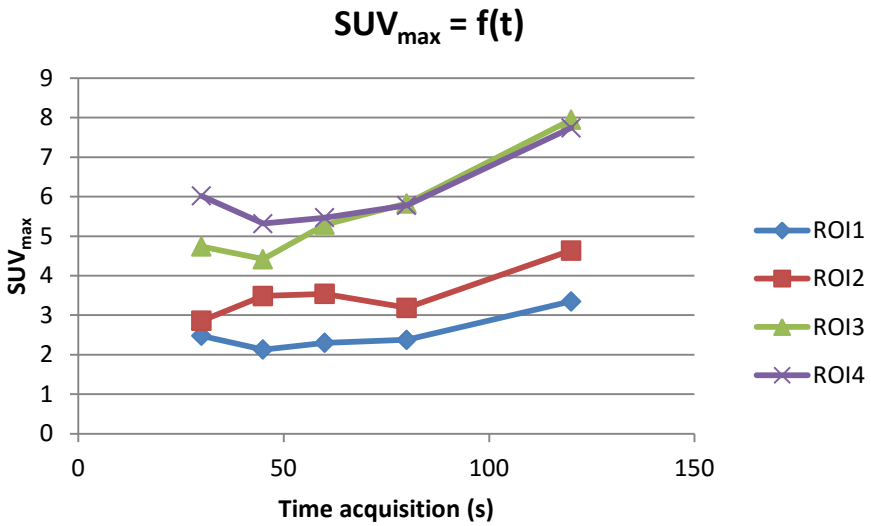

Figure 25. SUV_{max} for the different ROIs as a function of the acquisition time.

Pooled correlations between the SUV measurements (mean and maximum) for the different acquisition time are shown in figures Figure 26 to Figure 33.

In general, SUV_{mean} showed higher correlation between the different acquisition times and the common acquisition time per bed position (80 s) than SUV_{max}. Comparing Figure 26 to Figure 29 (SUV_{max}) and Figure 30 to Figure 33 (SUV_{mean}), a very strong uphill linear relationship is present in all of them, although it is stronger for longer acquisition times (60 and 120 s), especially 120 s.

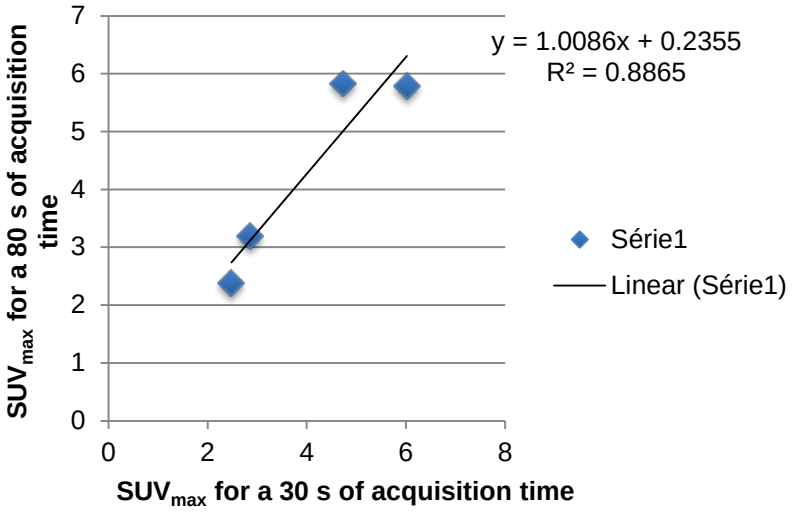

Figure 26. Correlation between SUV_{max} for 80 s and 30 s of acquisition time.

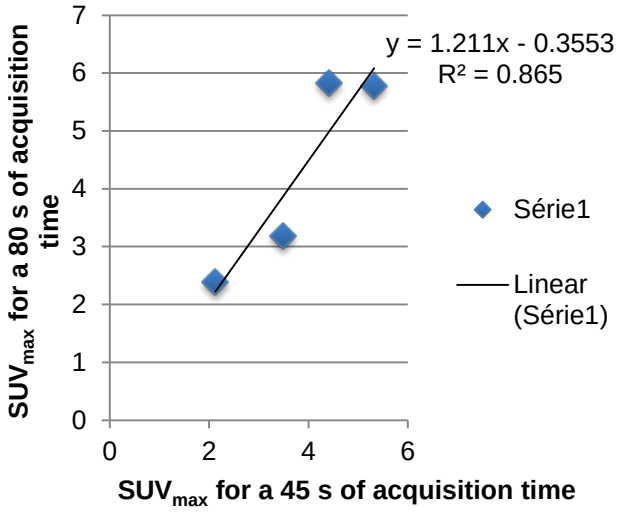

Figure 27. Correlation between SUV_{max} for 80 s and 45 s of acquisition time.

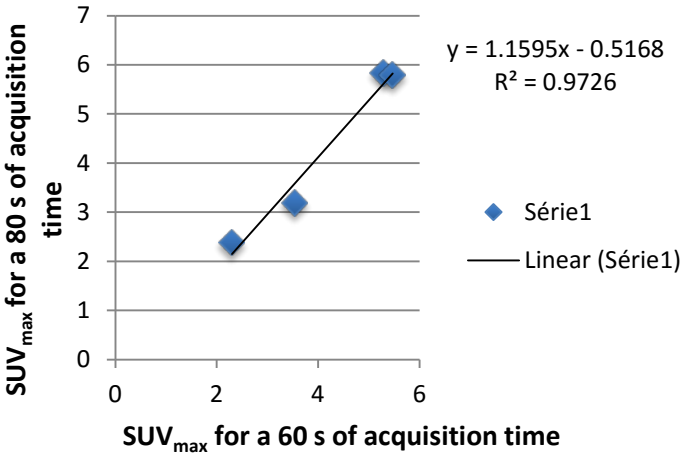

Figure 28. Correlation between SUV_{max} for 80 s and 60 s of acquisition time.

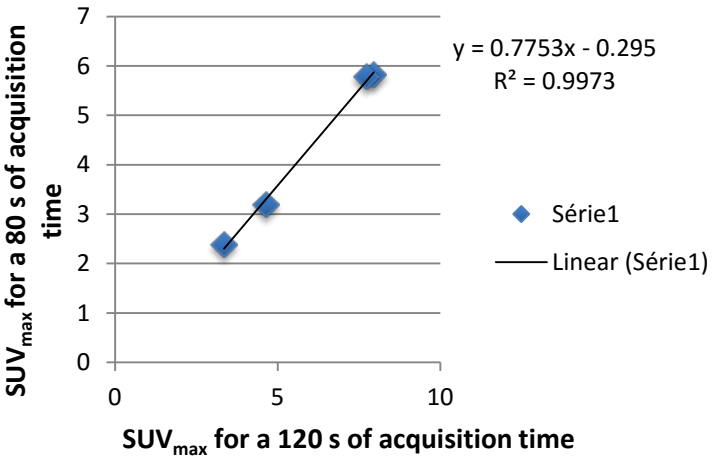

Figure 29. Correlation between SUV_{max} for 80 s and 120 s of acquisition time.

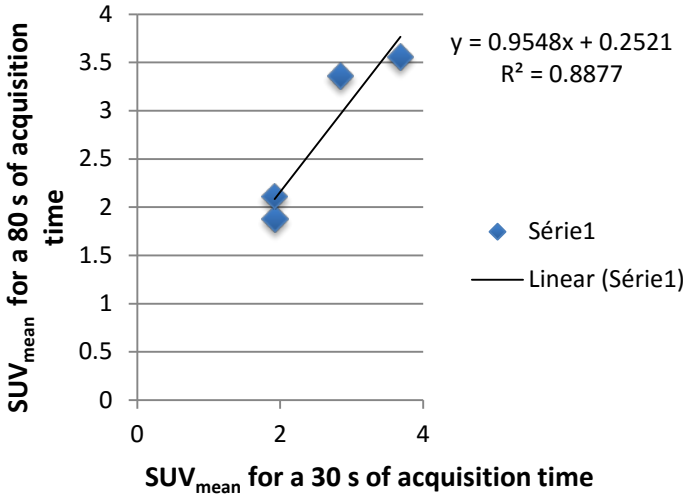

Figure 30. Correlation between SUV_{mean} for 80 s and 30 s of acquisition time.

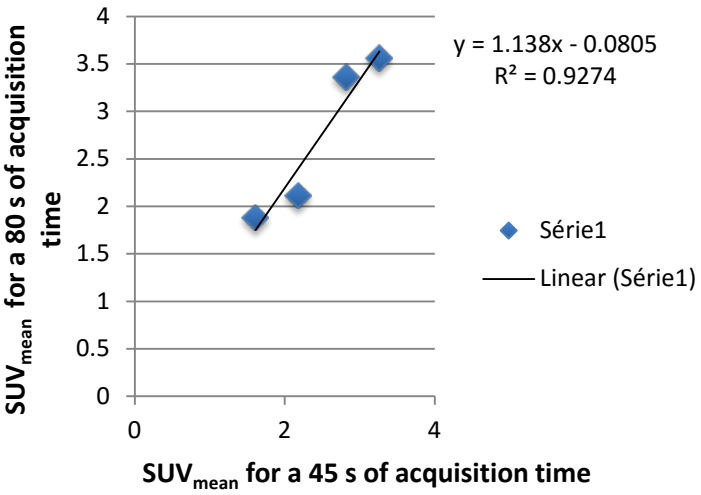

Figure 31. Correlation between SUV_{mean} for 80 s and 45 s of acquisition time.

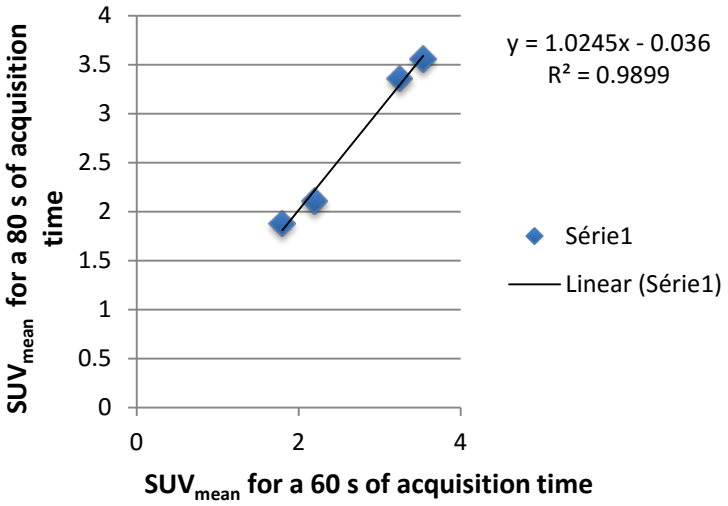

Figure 32. Correlation between SUV_{mean} for 80 s and 60 s of acquisition time.

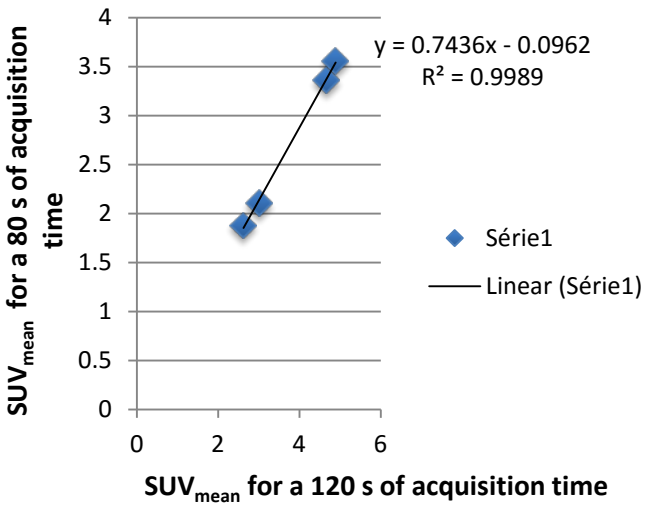

Figure 33. Correlation between SUV_{mean} for 80 s and 120 s of acquisition time.

As far as the SUV were concerned, *Pearson* correlation coefficients between different acquisition times and *p*-values for SUV_{max} and SUV_{mean} are as follows in Table 14 and Table 15, respectively.

There was a strong correlation for both SUV_{max} and SUV_{mean} between the different acquisition times ($R > 0.7$). For SUV_{max}, the lowest correlation was between 30 and 120 s ($R = 0.92799 \pm 0.06942$), which is reflected in 86.1% explained by the linear model applied. Correlation was higher between closer acquisition time as 80 and 120 s ($R = 0.99864 \pm 0.00136$) and 60 with 120 s ($R = 0.99028 \pm 0.00967$), which is reflected in 99.7% and 98.1%, respectively. For SUV_{mean}, correlation was lower between 30 and 120 s ($R = 0.93311 \pm 0.06466$) and 30 and 45 s ($R = 0.93419 \pm 0.06364$), which is reflected in 87.1% and 87.3%, respectively. Correlation was higher between 80 and 120 s ($R = 0.99943 \pm 0.00056$), 60 with 120 s ($R = 0.99609 \pm 0.00391$) and 60 and 80 s ($R = 0.99493 \pm 0.00505$), which is reflected in 99.9%, 99.2% and 99.0%, respectively.

Table 14. *Pearson* correlation coefficients matrix between the different acquisition times for SUV_{max} values.

		30 s	45 s	60 s	80 s	120 s
30 s	**R**	**1.**				
	R Standard Error					
	p-value					
45 s	**R**	**0.94717**	**1.**			
	R Standard Error	0.05144				
	p-value	0.05283				
60 s	**R**	**0.93521**	**0.97068**	**1.**		
	R Standard Error	0.06269	0.02889			
	p-value	0.06479	0.02932			
80 s	**R**	**0.94155**	**0.93004**	**0.98622**	**1.**	
	R Standard Error	0.05674	0.06751	0.01368		
	p-value	0.05845	0.06996	0.01378		
120 s	**R**	**0.92799**	**0.93222**	**0.99028**	**0.99864**	**1.**
	R Standard Error	0.06942	0.06549	0.00967	0.00136	
	p-value	0.07201	0.06778	0.00972	0.00136	

Table 15. *Pearson* correlation coefficients matrix between different acquisition times for SUV_{mean} values.

		30 s	45 s	60 s	80 s	120 s
30 s	**R**	**1.**				
	R Standard Error					
	p-value					
45 s	**R**	**0.93419**	**1.**			
	R Standard Error	0.06364				
	p-value	0.06581				
60 s	**R**	**0.94328**	**0.98502**	**1.**		
	R Standard Error	0.05511	0.01487			
	p-value	0.05672	0.01498			
80 s	**R**	**0.9422**	**0.96304**	**0.99493**	**1.**	
	R Standard Error	0.05613	0.03628	0.00505		
	p-value	0.0578	0.03696	0.00507		
120 s	**R**	**0.93311**	**0.96606**	**0.99609**	**0.99943**	**1.**
	R Standard Error	0.06466	0.03336	0.00391	0.00056	
	p-value	0.06689	0.03394	0.00391	0.00057	

The *t-test* was used to establish if the correlation coefficient is significantly different from zero, and, hence that there is evidence of an association between the two variables (two different acquisition times). There is then the underlying assumption that the data is from a normal distribution sampled randomly. The standard method that statisticians use to measure the 'significance' of their empirical analyses is the *p*-value. The *p*-value is a number between 0 and 1 representing the probability that this data would have arisen if the null hypothesis were true. A low *p*-value (0.05 in this study = 5% significance level) is taken as evidence that the null hypothesis can be 'rejected'. Statisticians say that a *p*-value of 0.05, or lower, is 'highly significant' or say that 'the data is significant at the 0.05 level'. In other words, the null hypothesis, H_0, relates to the statement being tested. In this study, H_0 is the hypothesis that different acquisition times per bed position generate significant differences in the SUV measurements (52).

There were no statistically significant differences between 30 s and the other acquisition times ($p > 0.05$) for both SUV_{max} and SUV_{mean}. The hypothesis H_0 was rejected between 60 and 45 s ($p = 0.02932$), 60 and 80 s ($p = 0.01378$), 60 and 120 s ($p = 0.00972$), 80 and 120 s ($p = 0.00136$) for SUV_{max} (Table 14). Table 15 shows statistically significant differences ($p < 0.05$) between all the acquisition times for SUV_{mean} (except for 30 s).

9.2.2. Patient imaging

From the patient imaging analysis, SUV_{max}, SUV_{mean} and standard deviation of SUVs are presented in Table 16. SUV_{max} is also shown in Figure 34 and SUV_{mean} in Figure 35.

Table 16. SUV values (mean and maximum) and correspondent standard deviation (σ_{SUV}) for the different tissues as a function of the acquisition time.

Acquisition time (s)	SUV_{max}			SUV_{mean}			σ_{SUV}		
	Liver	**Spleen**	**Bone**	**Liver**	**Spleen**	**Bone**	**Liver**	**Spleen**	**Bone**
30	6.32	12.64	4.86	2.55	5.67	0.47	1.11	1.61	0.82
45	11.19	7.74	0.99	3.32	4.60	0.35	1.52	1.36	0.24
60	6.07	10.01	0.25	2.64	5.23	0.04	1.12	1.81	0.05
80	4.97	8.77	1.26	3.42	6.56	0.65	0.56	0.99	0.23

Analysing Figure 34, SUV_{max} is lower in the bone ($0.25 < SUV_{max} < 4.86$). In the liver, SUV_{max} varies between 4.97 (80 s) and 11.19 (45 s) and in the spleen, SUV_{max} varies between 7.74 (45 s) and 12.64 (30 s). Although SUV_{max} is higher in the spleen, liver has higher SUV at 45 s.

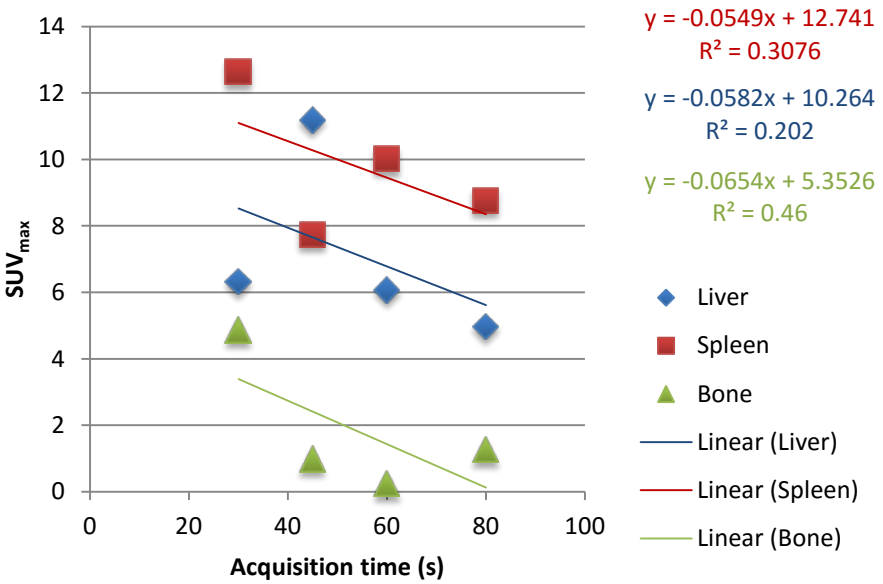

Figure 34. SUV_{max} for the different tissues as a function of the acquisition time.

Analysing Figure 35, SUV_{mean} is lower in the bone ($0.04 < SUV_{mean} < 0.65$). SUV_{mean} is higher in the spleen than in the liver for all the acquisition times. In the liver, SUV_{mean} varies between 2.55 (30 s) and 3.42 (80 s) and in the spleen, SUV_{mean} varies between 4.60 (45 s) and 6.56 (80 s).

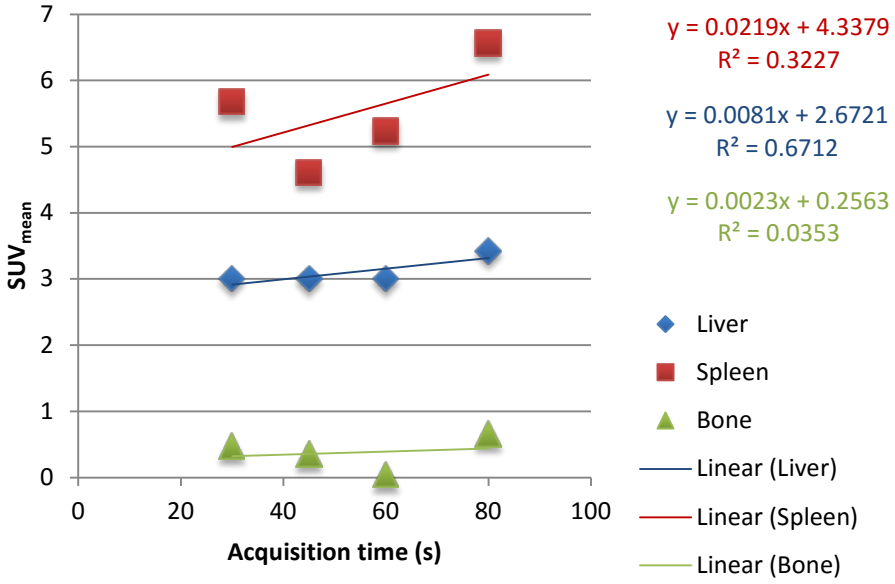

Figure 35. SUV_{mean} for the different tissues as a function of the acquisition time.

The standard errors measurements between the different acquisition times and the acquisition time per bed position commonly used in clinical PET/CT scanners at the Nuclear Medicine service of *Champalimaud Foundation* (80 s) for both SUV_{max} and SUV_{mean} are shown in Table 17. In general, percentage errors were not significant different between the acquisition times, except for liver (45 *vs* 80 s) and bone (30 *vs* 80 s) in SUV_{max} (liver: 125%; bone: 286%). Between the different tissues, spleen has a lower PE for SUV_{max} and liver has a lower PE for SUV_{mean}.

Table 17. PE values between the different acquisition times for SUV_{max} and SUV_{mean}.

		30 *vs* 80 s	**45 *vs* 80 s**	**60 *vs* 80 s**
SUV_{max}	Liver	27 %	125 %	22 %
	Spleen	44 %	12 %	14 %
	Bone	286 %	21 %	80 %
SUV_{mean}	Liver	25 %	3 %	23 %
	Spleen	14 %	30 %	20 %
	Bone	28 %	46 %	94 %

10. Discussion

Nowadays, there is a wide variety of medical imaging modalities that allow the study of the morphology and function of many systems of the human body. However, the intrinsic characteristics from the obtained images and their complexity often require computational methods. That is why there are several techniques of image processing able to assist in the extraction of relevant information (53).

10.1. Image quality parameters

10.1.1. Phantom imaging

All the hot spheres were noticeable for all the acquisition times. This event can be related with spatial resolution. The equipment is capable of detecting point sources up to 4.8 mm and the smallest sphere has a significant superior diameter (10 mm). The phantom spheres are more distinguishable from the background as time acquisition increases, which mean that images become sharper over time. The sharpening term can enhance the edges of the image. This enhancement happens because a higher number of counts is collected during larger acquisition times, causing the acquired image more similar to the real object (23) (54).

The quantification of radionuclide distribution has been a goal since the early days of nuclear medicine. A variety of types of quantitative values can be extracted from nuclear medicine images. PET has always been considered a quantitative imaging modality since it has the potential to precisely estimate local concentration of the radiotracer and since meaningful physiological parameters can be derived from these local concentration values. This technique has been widely used in oncology studies for the detection and the quantification of abnormal uptake (23).

The ROIs were defined semi-automatic. For that, an automatic algorithm is used to define region, but needs operator assistance to adjust the contours found by this algorithm. The quantitative measurements can be strongly dependent on the method used to define the regions. Moreover, it is important to refer that the detection probabilities are random and independent, so the number of counts recorded by radiation detectors in nuclear medicine systems is governed by a *Poisson* distribution, due to the detection of rare events (23).

In general, the quality of an image can be described quantitatively by its SNR. The SNR directly affects diagnostic and quantitative accuracy. In essence, then, a major goal of nuclear medicine equipment is to maximize the SNR in an image. Signal-to-noise ratios are indicators of the visual utility of an image for detection purposes (55). The SNR describes the relative strength between the desired information and the noise in the image. The higher the SNR, the less obtrusive the noise is. The value SNR = 5 is the conventional value of detectability used in radiology, and has also been used in emission tomography images. Regions for which $T-B>5\sigma_B$ can be considered 100% visible (12) (41). According to the data collected, all the four spheres were 100% visible for all the acquisition times. Nonetheless, only the smallest sphere (sphere corresponding to ROI_1) showed a SNR > 5. SNR values for the lower sphere activity concentration are in the vast majority of situations higher than the 100% detectability limit. This can be related with iterative reconstruction methods providing a better SNR in regions of low tracer uptake. In some cases, the smallest sphere diameter tends to converge to higher SNR values than for highest sphere diameter. Once this parameter describes a ratio between signal and noise, higher SNR means that there is a larger difference between these values (desired information is much superior to noise), which do not imply better signal. In other words, it is possible to have a high SNR with low signal, since noise compensates it, being much lower. It was observed that noise increased for bigger spheres, which results in an increase of the SNR value for smaller spheres. In the field of image processing, if an image possesses high SNR, it alone cannot be declared much useful unless there exists a high enough CNR ratio too (42).

Noise represents the existence of a random natural signal that confers a different appearance from the expected in medical image. Natural radioactivity, patients in neighbouring rooms or corridors and residual radioactivity can result in background radiation. Thereat larger acquisition times make the acquired object more similar to the real object. There are two types of noises: the random noise that interacts with the image receptor and can be controlled by the practitioner (increasing the administered activity or the acquisition time); the scattered radiation (non-random variations in counting rate) that cannot be controlled by the practitioner (54). For low count studies, this can have significant contribution to measured data and result in degraded quantitative information. In nuclear medicine, noise results from random nature of the radioactive decay process. Each atom of a radionuclide has the same probability of decay, which is independent of time and the probability of decay for each atom is independent of other atoms. The decay is managed by *Poisson* statistics for a large number of atoms (23). Noise is a function of accumulated counts and it is related to the efficiency of the detection system and injected activity. Once the activity concentration was the same for the hot spheres in this study, sensitivity highly influences image noise. The fact that noise increases with longer acquisition times is related

with the increase of counts number per unit time detected by the equipment. Also, noise increases for larger spheres, generally, due to a higher amount of variation of the counts number (standard deviation). The variance is proportional to the sensitivity of the imaging system, the activity of the source and the acquisition duration. It is also affected by factors that change the number of photons counted including attenuation, scatter and count rate losses (54). Furthermore, the presence of background activity causes noise and contrast loss in PET images (42). Noise can be reduced by reducing the number of updates, low pass post-reconstruction filtering of the reconstructed images or by increasing the smoothing on the reconstruction filter for filtered back projection methods. However, reducing noise is usually associated with a reduction in the spatial resolution of the reconstructed activity distribution and an increase of PVEs, introducing potential biases when quantifying activity concentration in small structures (23).

Contrast is related with the differences in image intensity between different tissues (39). This parameter not only depends on the number of counts, but also on the size of the ROI. The increased ROI contrast produces a significant increase on the standard deviation (contributing for the increase of noise) of the mean signal recover, leading to a decrease in SNR and CNR (42). Higher contrast values are often related with noisier images (both are localized in high frequencies). It is expected that a better contrast is near to 100%. Based on this, only the two larger hot spheres (corresponding to ROI_3 and ROI_4) have relatively a good contrast (> 50%) for the different acquisition times. In this study, the spheres with 1.7 and 2.2 cm of diameter have a contrast higher than 50% for 45, 60, 80 and 120 s. For 30 s, the contrast is superior to 50% in the sphere with 2.2 cm.

The CNR refers to the ability in PET to distinguish between various contrasts in an acquired image and the inherent noise in the image (55). CNR is used as a measure for assessing the ability of an imaging system to generate clinically useful image contrast. The measure of image contrast only is not precise enough to qualify an image. We need contrast ratio to noise in order to have a better measure of the image quality as compared to that of SNR. The CNR is more suitable for those images, which possess a significant amount of bias, such as haze. We can say that it gives an objective measure of useful contrast. A higher CNR value is necessary in order to distinguish among different tissue types, and in particular between a healthy tissue and a pathological tissue. Moreover, when the size of a sphere is substantially larger than the limiting spatial resolution it can influence the detection ability, especially if the sphere has low contrast. From the obtained results, CNR improves significantly as the sphere contrast decreases (42).

For activity quantification of small targets such as tumours, recovery coefficients can be used. These coefficients are usually determined from phantom experiments with spherical sources of known sizes and activity contents and similar acquisition conditions. The recovery

coefficient is a functional of the object shape, size, activity relative to the background[10] and the position in the image (due to the spatially varying resolution). Due to the number of variables, recovery coefficients are typically tabulated only as function of object size (23).

Concerning the contrast recovery coefficient (CRC), the evaluation of it indicates how reliable the reconstructed image would be for detection tasks in real situations. This result in the ability to evaluate the reconstruction algorithm used to recover a certain simulated contrast between a hot sphere (NEMA phantom) and a background. In practice, this contrast is provided by the radiotracers distribution. The goal of the imaging system is to preserve this contrast in the image. Contrast is maintained by avoiding blurring, which smears counts from higher activity regions into lower activity regions (and vice versa), thus reducing image contrast. In this way, spatial resolution and contrast are closely linked (42) (43). This measurement was similar to contrast, although CRC has into account the injected activity, which is why these parameters produce a similar behaviour for the different spheres of the phantom and acquisition times. According to other studies using ^{18}F-FDG (18) (19) (43), higher values of CRC were obtained for larger spheres and for longer acquisition times, which is consistent with this study.

Although, the volume recovery coefficient (VRC) is not directly considered a parameter of image quality analysis, it has a major role. This parameter is useful to verify if the measured volume is similar to the real volume of the spheres, so that possible errors can be inferior. In this study, the volumes of spheres were overestimated, especially for sphere 2 (about twice) – ROI_2. This can be related with the fact that were used ROIs instead of volumes of interest (VOIs). The volumes of the spheres were calculated from the measured diameter and compared with the real ones, perhaps decreasing its sensibility (23) (42).

It should be taken into consideration that the characteristics of the equipment (such dead time, sensibility, spatial resolution, timing resolution, and energy resolution) will have influence on the obtained results. In order to provide a suitable precision of the measurements, data should be acquired for long enough at each time. Data points should be acquired over a time that is long enough so that the observed count rate is in the range where count rate losses are small (23).

[10] Radionuclides undergo radioactive decay resulting in reduced activity as a function of time. For quantitative tasks it is important to account for this effect (23).

10.1.2. Patient imaging

PSMA is a cell surface protein with high expression in prostate carcinoma cells. The normal distribution of ^{68}Ga-PSMA includes kidneys and urinary bladder (intense tracer uptake), salivary glands, lacrimal glands, liver, spleen and small and large bowel (moderate tracer uptake) (56). Low tracer uptake is present in normal bone marrow (57). The intensive uptake in the kidneys and bladder is related with the urinary excretion (57). After the excretory organs, spleen, salivary glands and liver are the organs with higher dosimetry (respectively) (57), reason why liver and spleen were chosen for this study and bone marrow for background. The chosen slice for this study was positioned in the upper abdominal in order to cover different tissues, namely, liver, spleen and bone marrow.

Since the acquisition time per bed position commonly used in clinical PET/CT is 80 seconds at the Nuclear Medicine service of *Champalimaud Foundation* and the main aim of this dissertation is to decrease the acquisition time per bed without compromising the image quality, a time per bed of 120 s was not performed. In addition, there were not detected significant differences between 80 and 120 s with the phantom results.

In the second phase of this study (patient acquisition), CRC and VRC were not analysed. Recovery coefficients are generally used to quantify small lesions (for example, tumours) (23). Besides this, CRC was not calculated in patient images, since it has into account the activities inserted in the object and for the background. VRC was not calculated, since there were not found any lesions in the selected slices to compare the measured volume with the real one.

Some investigators (56) (57) concluded that at 60 min after radiotracer injection the contrast of acquired images is better than earlier or later images. However, in the present study, images were only possible to acquire after 90 min after injection.

Images for 80 s per bed position are clearer, comparing with the other acquisition times (30, 45 and 60 s), most probably because it was acquired approximately 45 min before the others (in order to not interfere with the dynamic of the service).

In general, spleen showed higher SNR, contrast (and consequently, noise) and CNR than liver, which is consistent with the studies mentioned before (56) (57). It is assumed that detectability is expected when SNR ≥ 5 (12) (41). In this case, only liver exhibits a high SNR value for 80 s (SNR = 6.31). On the other hand, contrast decreased for 80 s in both liver and spleen. Despite that, high contrast (> 50%) was observed in both liver and spleen for all the acquisition times (30, 45, 60 and 80 s). Noise increased with longer acquisition times, which is also related with the increase of counts number per unit time detected by the equipment.

The ratio between contrast and noise (CNR) showed also good results with higher values in the spleen and a similar behaviour for 30, 45 and 60 s.

As expected, these image quality parameters revealed better results with longer acquisition times. However, there were not detected significant differences between 30, 45 and 60 seconds. This proposition can be sustained with the obtained PE values.

Although the patient did not present any lesions in the acquired slice, the measurements obtained with the clinic image were compared with the ones obtained with the NEMA phantom. Comparing these results, the phantom showed more consistency on the measurements (more similar values of the image quality parameters for the different acquisition times). This fact can be sustained by analysing PE values. There are more errors between the different acquisition times in clinical images (40% ± 0.23) than in phantom images (15% ± 0.10). However, contrast values obtained in clinical images are much better than the ones obtained with phantom images. This comparison is not righteous, since we are comparing organs with lesion simulations (spheres) and the concentrations in the objects are not the same. Moreover, there are some characteristics related to the patient that can influence the obtained results and make the image far from the ideal (artifacts). Artifacts can be distinguished from noise, once they do not have a random nature. Artifacts represent information in the image that not necessarily exists in the object. These phenomena are caused by physiology variability, background noise (internal or external), the equipment (lack of calibration) or electronic noise (54).

In patient imaging, there are some factors that should be taking into account, such as scatter photons, attenuation, motion (especially for small objects), PVE and patient thickness (23). The spatially varying resolution reduces the contrast of the objects near the centre of rotation as a result of increased PVEs (23). Physiological (involuntary motion (cardiac and respiratory) and voluntary motion (patient moving during the scan) adversely affect the quantitative accuracy of PET or PET/CT images (23). These effects can be quite severe depending on the respiratory amplitude and tumour size, with SUV underestimation and tumour volume overestimation greater than 20% (23), although it is not relevant in this case. As to overcome this disadvantage, images can be acquired using (cardiac and respiratory) gating. Due to the relatively long duration of PET acquisition, involuntary motion can also affect the measured data, resulting in inconsistent projection data (23).

10.2. SUV

10.2.1. Phantom imaging

SUV is especially used for patient monitoring, to determine whether tumours respond to therapy (over the course or at the end of the treatment). SUV can integrate noise, especially when calculated from the maximum pixel value in a tumour region. The highest SUV (SUV_{max}) is calculated using the highest voxel value in the tumour. The mean SUV measured over a ROI is more robust to noise, but might be biased by PVEs if the tumour is small (typically less than 3 times the spatial resolution in the reconstructed images) (23).

PVE refers to the fact that a pixel includes a mixture of signals coming from different sources. PVE introduces quantitative biases. Even if the spatial resolution were ideal, PVE would still occur owing to image sampling (counts from other tissues, for example). The larger the voxel, the greater this effect. PVE can introduce significant biases (> 50%) when assessing the tumour uptake (SUV) in small tumours. Partial volume correction (PVC) is not used or available in current clinical practice, although it is considered important for quantifying activity in small objects such as tumours. Estimate the activity concentration of the object (using a ROI) is one used method to reduce PVEs, especially in the estimation of tumours SUV (23).

In terms of SUV_{max}, there is not a consensual value that distinguishes an abnormal uptake from a normal uptake, especially for ^{68}Ga labelled radiopharmaceuticals. For ^{18}F-FDG, SUVs can go from <1 (soft tissues) to 3.5 (renal cortex) in normal tissues. SUVs in neoplastic tissues stand between 2 and 25 (1). Kratochwil *et al.* (2015) suggest a threshold value of >16.4 for SUV_{max} in studies with ^{68}Ga-DOTATOC to select patients for peptide receptor radiation therapy (58). In other study with ^{68}Ga-DOTATOC, a threshold for SUV_{max} between 0.84 and 1.47 was found in normal tissues and between 3.24 and 9.1 in malignant tumours (59). In the present study, SUV_{max} varies between 1.1 (45 s) and 1.6 (120 s) for the background (normal tissue) and between 2.1 (ROI_1, 45 s) and 8.0 (ROI_3, 120 s) for the hot spheres (abnormal uptake), which is consistent. It should be taken into account that both acquisition time and the ROIs size influence the standardized uptake value.

Correlations are useful measures of the strength and direction of association that exists between variables. In this case, it was observed a strong and positive association between the acquisition times for SUV_{max} (≥ 86.1%) and SUV_{mean} (≥ 87.1%), suggesting that SUVs are similar between the commonly used acquisition time per bed position (80 s) and the shorter acquisition times proposed in the study (30, 45 and 60 s).

The hypothesis that different acquisition times per bed position generate significant differences in the SUV measurements was studied. This hypothesis was verified between 30 s and the other acquisition times (45, 60, 80 and 120 s), between 45 and 80 s and between 45 and 120 s, which means that there were statistically significant differences between shorter and longer acquisition times for SUV_{max}. For SUV_{mean}, the hypothesis was verified only between 30 s and the rest of acquisition times (45, 60, 80 and 120 s), meaning that statistically significant differences were found only for the shorter acquisition time (30 s).

10.2.2. Patient imaging

In the second phase of this study (patient imaging), Pearson correlation and *t-test* were not applied. These parameters are useful to analyse and compare variables, investigating if there are differences between them. On phantom imaging, this was appropriate, since the four spheres were injected with the same activity concentration and the main objective was to compare if there were significant differences between them with different acquisition times. In the case of clinical imaging, there are not visible lesions and organs have mandatorily different dose concentrations, which is why Pearson correlation and *t-test* were not applied in this specific case.

As referred in subchapter 5.2. of chapter II, SUV_{max} is related with the SUV of the maximum intensity voxel within a ROI, while SUV_{mean} is the average measure of SUV within calculated boundaries of a tumour (44). Although SUV_{max} is more used than SUV_{mean} in the clinical practices, SUV_{mean} showed more stable values. The ideal SUVs keep constant with different acquisition times or, at least, increase with longer acquisition times. In the present study, this was only verified for SUV_{mean}. On the other hand, it is expected that the uptake decreases in benign tissues over time, due to the normal clearance, as opposed to the uptake in tumour lesions (uptake of radiotracer in abnormal lesions increases over time) (60).

Herrmann *et al.* (2015) found that median SUV_{max} = 55.0 (with ^{68}Ga-PSMA) in the primary prostate cancer at 1h after injection, SUV_{max} = 57.0 in iliacal lymph node metastases and SUV_{max} = 31.4 in mediastinal lymph node metastases (57). Prasad *et al.* (2016), found a median SUV_{max} = 3.2 for non-pathological uptake in lymph nodes and SUV_{max} = 1.9 for non-pathological uptake in bones (61). According the present study, median SUV_{max} = 7.1 for liver, SUV_{max} = 9.8 for spleen and SUV_{max} = 1.8 for bone, considering all the acquisition times. Although SUV_{max} were not analysed for liver and spleen in those studies or in other available ones, results are consistent for bone (1.8 *vs* 1.9). Spleen shows a higher SUV_{max} than liver,

which is consistent with the results obtain in other studies referred before (subsubchapter 10.1.2. of chapter III) for absorbed doses (56) (57).

Percent errors were minor for SUV_{mean} (31% ± 0.26) than for SUV_{max} (70% ± 0.89). If the two outliers (125% for liver and 286% for bone) were ignored, PE values for SUV_{max} would be equivalent to SUV_{mean} (31% ± 0.24). PEs are useful to investigate the error dispersion (42) between the common acquisition time per bed position (80 s) and the different acquisition times for each tissue. SUV_{max} at 45 s in the liver is over 2 times higher than at 80 s. As well as SUV_{max} at 30 s in the bone is almost 4 times higher than at 80 s. The SUV_{mean} is more robust to noise, reflecting more stable results (23).

It is important to refer that liver usually does not show an homogenous uptake and images with 30, 45 and 60 s per bed were acquired almost 2 h after injection. Since half-life of ^{68}Ga is approximately 1 h, organs contained half of the dose at 2 h, which can explain the dispersion between SUVs (especially SUV_{max}).

Like what happens with image quality parameters, SUV can be influenced by several intrinsic or extrinsic factors to the patient, previously reported in subsubchapter 10.1.2. of chapter III. Furthermore, SUV can be affected by other biological factors, such as uptake period, that cannot be controlled by the technician. Technical factors that can be controlled by the technician can also appear, like relative calibration between PET scanner and dose calibrator, residual activity in syringe, incorrect synchronisation of clocks, injection *vs* calibration time and quality of administration. Physical/data analysis-related are other possible factors (controlled by the technician) that can occur: scan acquisition parameters and image reconstruction parameters (5).

11. Conclusion

PET has been a major modality in oncology for diagnostic, staging and evaluation to treatment response of tumours. TOF PET scanners enable an improvement SNR and decrease of random coincidences, allowing better contrast, especially for large patients, improving structural details and leading to a short scan time.

All the four hot spheres were 100% visible for all the acquisition times.

SNR was higher for the smallest hot sphere (1 cm), indicating that iterative reconstruction methods compensate SNR in smaller regions and/or with low tracer uptake. Furthermore, a higher SNR does not mean a better signal, but a larger positive desired information/noise ratio. The fact that images with shorter acquisition time show higher SNR seems to indicate that the SNR = 5 criterion, from conventional radiology, might not be indicate for emission tomography images.

Noise increases in larger spheres and with longer acquisition times, which implies an increase of the SNR and CNR values for smaller spheres and shorter acquisition times. This is related with a higher variation of counts (standard deviation) and the increase of counts number per unit time detected by the equipment, respectively. Noisier images are often related with higher contrast values, since both are localized in high frequencies.

A contrast above 50% was verified in the largest hot sphere (2.2 cm) for all the acquisition times and also in the second largest hot sphere (1.7 cm) for acquisition times longer than 30 s (45, 60, 80 and 120 s).

As SNR, CNR was higher for the smallest hot sphere.

CRC showed a similar behaviour to contrast for the different spheres sizes and acquisition times. The major difference between these parameters is the weighting of the injected activity for CRC that is despised for contrast measurement.

VRC was overestimated, especially for sphere 2 (about twice), suggesting that VOIs should be made instead of ROIs, decreasing quantitative bias.

SUV_{max} values are typically used for abnormal lesions. There is not a consensual value that distinguishes an abnormal uptake from a normal uptake, especially for ^{68}Ga labelled radiopharmaceuticals. Nonetheless, obtained SUVs measurements were in accordance to other studies. SUV_{max} varied between 1.1 and 1.6 for the background (normal tissue) and between 2.1 (ROI_1, 45 s) and 8.0 (ROI_3, 120 s) for the hot spheres of the NEMA phantom (abnormal uptake). Correlations were very strong and positive for SUV_{max} and SUV_{mean} between the different acquisition times (≥ 86.1% and ≥ 87.1%, respectively), suggesting that

SUVs measurements are similar between the commonly used acquisition time per bed position (80 s) and the shorter acquisition times proposed in the study (30, 45 and 60 s). There were statistically significant differences ($p < 0.05$) between shorter and longer acquisition times (between 30 s and the other acquisition times, between 45 and 80 s and between 45 and 120 s) for SUV_{max}. There were statistically significant differences between the shorter acquisition time (30 s) and the rest of acquisition times for SUV_{mean}.

Image quality parameters revealed better results with longer acquisition times in patient imaging also. However, there were not detected significant differences between 30, 45 and 60 seconds. Spleen showed higher SNR, contrast, noise and CNR than liver. A SNR ≥ 5 was only verified for 80 s on the liver. High contrast (> 50%) was observed in both liver and spleen for all the acquisition times (30, 45, 60 and 80 s). Noise increased with longer acquisition times, which is also related with the increase of counts number per unit time detected by the equipment. CNR showed also good results with higher values in the spleen and a similar behaviour for 30, 45 and 60 s.

More consistent image quality parameters values were observed in the phantom imaging than in the patient imaging with a PE of 15% ± 0.10 and 40% ± 0.23, respectively. However, contrast was higher on patient imaging.

SUV_{mean} showed more stable values (31% ± 0.26) than SUV_{max} (70% ± 0.89) in patient imaging. The SUV_{mean} is more robust to noise, reflecting more stable results. Median SUV_{max} was 7.1 for liver, 9.8 for spleen and 1.8 for bone, considering all the acquisition times (30, 45, 60 and 80 s).

It should be not forgotten that results obtained with phantoms are more predictable than with clinical images. There are several factors associated to patients that technicians cannot control, such as physiology variability, scatter photons, attenuation, patient thickness and motion.

Concluding, image quality increases with longer acquisition times per bed. It is feasible to decrease the acquisition time to below 2 min per bed position without compromising the spheres detection, of the NEMA phantom, rate and diagnostic image quality. Considering the quantification in terms of radioactivity uptake (SUV), it is possible to decrease the acquisition time to 45 s. However, in the case of phantom imaging, the PE for all the image quality parameters increases with the decrease of time and ROI size, whereby a time of 60 s per bed is proposed for future clinical practices, in order to not lose information in the quantification of small regions.

Chapter V – Final considerations and future perspectives

12. Final considerations and future perspectives

The objectives of the study were all accomplished and there were no ethical conflicts to declare. As difficulties of the study, we found a rareness of needles sufficiently long to get in the spheres of the NEMA phantom (especially the two smallest), overcome non-recognition of images by some software programs (not import data sets from files) and finding patients with lesions.

In nuclear medicine, hot lesions prevail over cold lesions, reason why we selected more hot spheres (4/6) than cold spheres. We also chose the four smallest spheres to simulate hot lesions, in order to realise what is the minimum detectable lesion size.

Decreasing acquisition time per bed from 80 s to 60 s or 45 s reflects a significant decrease on the total scan time, approximately, from 13 min to 7-10 min (depending on the number of beds). Thus, patients will feel more comfortable, probability of motion will be lower and, consequently, artifacts generation, persevering the image quality. Additionally, more scans per day can be scheduled and decreases the number of patients waiting to do the scan, contributing for an optimization of the protocols.

In the near future, a large sample should be collected for patient imaging (with lesions). Also, it should be done a new acquisition on the phantom with different activity concentrations in the spheres, in order to simulate different tissues of the human body (comparison between phantom and patient imaging more feasible). Evaluate the influence of the injected activity to the image quality in TOF PET scanners should also be considered. The advantages of this technique lead to a short scan time or injected dose. The scan time was studied in this thesis, remaining lacking how injected dose can influence the image quality in TOF PET scanners. The benefits of TOF at the image quality using ^{68}Ga citrate and how it translates into improved performance for patient imaging should also be investigated. A protocol with standard operating procedures should be written for any quantitative imaging task by a team of physicists, medical staff and technologists, ensuring consistency of data acquisition and processing. Also, a matrix of SUVs for normal tissues and another for different abnormal uptakes (for different tissues) should be reached for the radiopharmaceuticals used in PET.

References

1. Vaz TR. Avaliação do Desempenho de um Sistema Híbrido de Tomografia por Emissão de Positrões e Tomografia Computorizada (Performance Evaluation oh a hybrid system of PET/CT). 2013. Master's thesis in Nuclear Medicine in Escola Superior de Tecnologia da Saúde de Lisboa.
2. Karp JS. Time-of-Flight PET. PET Center of Excellence Newsletter. 2006; 3.
3. Surti S, Kuhn A, Werner M, Perkins A, Kolthammer J, Karp J. Performance of Philips Gemini TF PET/CT Scanner with Special Consideration for Its Time-of-Flight Imaging Capabilities. The Journal of Nuclear Medicine. 2007 March; 48.
4. Smith TJ. Time-of-Flight PET Compared to Increased Scan Time in Low-Contrast Regions. 2011. Thesis of Master's degree of Science in the Graduate Program in Medical Physics in the Graduate School of Duke University.
5. Hogg P, Testanera G, Dennan S, Heathcote A, Kane T, Wareing A, et al. Principles and Practice of PET/CT Hogg P, Testanera G, editors. Austria: European Association of Nuclear Medicine; 2010.
6. From matter to radioactive nuclei. [Online]. [cited 2016 January. Available from: http://www.ganil-spiral2.eu/science-us/understand-ganil/fundamental-principles.
7. Radioactive decay and radioactivity. [Online].; 1999 [cited 2016 January. Available from: http://physics.bu.edu/~duffy/py106/Radioactivity.html.
8. Evans RD. The Atomic Nucleus New York: McGraw-Hill; 1955.
9. Kramer EL, Ko JP, Ponzo F, Mourtzikos K. Positron Emission Tomography/Computed Tomography: A Disease-Oriented Approach Kramer EL, Ko JP, Ponzo F, Mourtzikos K, editors. New York: Informa Healthcare USA, Inc.; 2008.
10. Multimodal NeuroImaging Analysis. [Online].; 2015 [cited 2016 March. Available from: https://multimodalneuroimaging.wordpress.com/2015/04/28/c-positron-emission-tomography/.
11. Alessio AM, Butterworth E, Caldwell JH, Bassingthwaighte JB. Quantitative imaging of coronary blood flow. [Online].; 2010 [cited 2016 March. Available from: http://www.nanoreviewsexperiments.net/index.php/nano/article/view/5110.
12. Cherry SR, Sorenson JA, Phelps ME. Physics in Nuclear Medicine. Fourth edition ed. Philadelphia: Elsevier; 2012.

13. [Online]. [cited 2015 November. Available from: http://www.globalsecurity.org/wmd/library/policy/army/fm/8-9/1ch2.htm.
14. Saha GB. Performance Characteristics of PET Scanners. In Basics of PET Imaging: Physics, Chemistry, and Regulations.: Springer; 2010. p. 97-116.
15. Hussain S. A Simple PET Imaging Educational Demonstrator. 2012. Master of Science Thesis in Medical Engineering (Stockholm).
16. Schmitz RE, Alessio AM, Kinahan PE. The Physics of PET/CT scanners. [Online]. [cited 2015 October. Available from: http://depts.washington.edu/imreslab/education/Physics%20of%20PET.pdf.
17. Jani P, Vámos L, Nemes T. Timing resolution (FWHM) of some photon counting detectors and electronic circuitry. Meas. Sci. Technol. 2006 November: p. 155-160.
18. Surti S. Update on Time-of-Flight PET Imaging. The Journal of Nuclear Medicine. 2015 January; 56.
19. Karp JS, Surti S, Daube-Witherspoon ME, Muehllehner G. The benefit of time-of-flight in PET imaging: Experimental and clinical results. J Nucl Med. 2008 March; 49.
20. Fahey FH. Data Acquisition in PET Imaging. Journal of Nuclear Medicine Technology. 2002 June; 30.
21. Brasse D, Kinahan PE, Lartizien C, Comtat C, Casey M, Michel C. Correction Methods for Random Coincidences in Fully 3D Whole-Body PET: Impact on Data and Image Quality. The Journal of Nuclear Medicine. 2005 May; 46.
22. Tong S, Alessio AM, Kinahan PE. Image reconstruction for PET/CT scanners: past achievements and future challenges. Imaging Med. 2010 October: p. 529–545.
23. Buvat I, du Raan H, Frey EC, Green AJ, Hutton B, Ljungberg M, et al. Quantitative Nuclear Medicine Imaging: Concepts, Requirements and Methods. In IAEA Human Health Reports No. 9; 2014; Vienna. p. 1-57.
24. Biersack HJ, Freeman LM. Clinical Nuclear Medicine Germany: Springer Science & Business; 2008.
25. Tarantola G, Zito F, Gerundini P. PET Instrumentation and Reconstruction Algorithms in Whole-Body Applications. The Journal of Nuclear Medicine. 2003 May; 44.
26. Wilson JM. Parameterizing Image Quality of TOF versus Non-TOF PET as a Function of Body Size. 2011. Dissertation in the Graduate Program in Medical Physics of Duke University.
27. Research Gate. [Online]. [cited 2016 January. Available from: https://www.researchgate.net/figure/232705432_fig5_Schematic-illustration-of-the-

differences-between-conventional-PET-top-and-TOF-PET.

28. Brix G, Dondi M, Malone J, Mantil J, O'Reilly G, Rehani MM, et al. Radiation Protection in Newer Medical Imaging Techniques: PET/CT Brix G, Dondi M, Malone J, Mantil J, O'Reilly G, Rehani MM, et al., editors. Vienna: International Atomic Energy Agency; 2008.
29. Bomanji JB, Papathanasiou ND. Chapter 1 - Principles of PET radiochemistry: 68Ga-peptide tracers. In Testanera G, Broek WJ, editors. Principles and Practice of PET/CT - Part 2: A Technologist's Guide. Vienna: European Association of Nuclear Medicine; 2011. p. 32-42.
30. Virgolini I, Ambrosini V, Bomanji J, Baum R, Fanti S, Gabriel M, et al. Procedure guidelines for PET/CT tumour imaging with 68Ga-DOTA-conjugated peptides: 68Ga-DOTA-TOC, 68Ga-DOTA-NOC, 68Ga-DOTA-TATE. Eur J Nucl Med Mol Imaging. 2010 July; 37.
31. Mease RC, Foss CA, Pomper MG. PET imaging in prostate cancer: focus on prostate-specific membrane antigen. Curr Top Med Chem. 2013: p. 951-62.
32. Lapi SE, Publicover JG, Ruth TJ. Method for calibrating particle beam energy. [Online].; 2007 [cited 2015 August 14. Available from: http://www.google.com/patents/WO2007016783A1?cl=en.
33. Wadsaka W, Mitterhausera M. Basics and principles of radiopharmaceuticals for PET/CT. European Journal of Radiology. 2010 February; 73.
34. Doraiswamy PM, Sperling RA, Johnson K, Reiman EM, Wong TZ, Sabbagh MN, et al. Florbetapir F 18 amyloid PET and 36-month cognitive decline: a prospective multicenter study. Molecular Psychiatry. 2014 March: p. 1044–1051.
35. Nunes AT. Dose Optimization in CT, in Nuclear Medicine and in PET-CT Procedures. 2011. Thesis in the Master's Degree in Biomedical Engineering from the University of Coimbra.
36. Townsend D. Dual-Modality Imaging: Combining Anatomy and Function. The Journal of Nuclear Medicine. 2008 June; 49.
37. Munshi N. Imaging Evolution: Hybrid PET/CT Scans. 2012 May.
38. Wernick M, Aarsvold J. Emission Tomography: The Fundamentals of PET and SPECT: Elsevier Inc; 2004.
39. Branco S. Performance Measures and Quantitation in Molecular Imaging. 2015. Powerpoint presentation.
40. Kuni CC, Hasegawa BH, Hendee WR. Noise Reduction in Nuclear Medicine Images. The

Journal of Nuclear Medicine. 1983 February; 24.

41. Graham S, Links JM. Chapter 3: Instrumentation. In Christian PE, Waterstam-Rich KM. Nuclear Medicine and PET/CT Technology and Techniques. 6th ed.: Mosby Elsevier; 2007. p. 99-103.
42. Branco S. Small Animal PET Imaging Using GATE Monte Carlo Simulations: implementation of physiological and metabolic inormation. 2010. PhD Thesis in Biomedic and Biophysics Engineering by Faculdade de Ciências da Universidade de Lisboa.
43. Daube-Witherspoon ME, Karp JS, Casey ME, DiFilippo FP, Hines H, Muehllehner G, et al. PET Performance Measurements Using the NEMA NU 2-2001 Standard. The Journal of Nuclear Medicine. 2002 October; 43.
44. Carlier T, Bailly C. State-of-the-art and recent advances in quantification for therapeutic follow-up in oncology using PET. Frontiers in Medicine. 2015 March.
45. Boellaard R. Standards for PET Image Acquisition and Quantitative Data Analysis. The Journal of Nuclear Medicine. 2009 May; 50.
46. Soret M, Bacharach S, Buvat I. Partial-Volume Effect in PET Tumor Imaging. The Journal of Nuclear Medicine. 2007 June; 48.
47. Philips: GEMINI TF PET/CT. [Online]. [cited 2016 March. Available from: http://www.usa.philips.com/healthcare/product/HC882471/gemini-tf-pet-ct-scanner.
48. Norenberg P. Molecular Imaging: The Impact of the Ge-68/Ga-68 on Molecular Imaging. [Online].; 2013 [cited 2016 March. Available from: http://www.molecularimaging.net/topics/molecular-imaging/biomarkers/impact-ge-68ga-68-molecular-imaging.
49. Sroelov V. Gallium-68 (Ge-68/Ga-68). [Online]. [cited 2016 March. Available from: http://www.isotop.ru/en/production/medical/427/446/.
50. Biodex. PET Phantom - NEMA 2012/IEC 2008. [Online]. [cited 2016 March. Available from: http://www.biodex.com/nuclear-medicine/products/pet-positron-emission-tomography/pet-phantoms/pet-phantom-nema-2012iec-200.
51. Zanzonico P. Routine Quality Control of Clinical Nuclear Medicine Instrumentation: A Brief Review. The Journal of Nuclear Medicine. 2008 July; 49.
52. Velosa F, Pestana DD. Introdução à Probabilidade e à Estatística. 4th ed.: Fundação Calouste Gulbenkian; 2008.
53. Freire L. Técnicas de Image Enhancement. 2015. Powerpoint presentation.
54. Freire L. Fundamentos de Processamento de Imagem. 2015. Powerpoint presentation.
55. Sain JD, Barrett HH. Performance evaluation of a modular gamma camera using a

detectability index. The Journal of Nuclear Medicine. 2003; 44.

56. Afshar-Oromieh A, Malcher A, Eder M, Eisenhut M, Linhart HG, Hadaschik BA, et al. PET imaging with a [68Ga]gallium-labelled PSMA ligand for the diagnosis of prostate cancer: biodistribution in humans and first evaluation of tumour lesions. Eur J Nucl Med Mol Imaging. 2013 May; 40.
57. Herrmann K, Bluemel C, Weineisen M, Schottelius M, Wester H, Czernin J, et al. Biodistribution and Radiation Dosimetry for a Probe Targeting Prostate-Specific Membrane Antigen for Imaging and Therapy. The Journal of Nuclear Medicine. 2015 June; 56.
58. Kratochwil C, Stefanova M, Mavriopoulou E, Holland-Letz T, Dimitrakopoulou-Strauss A, Afshar-Oromieh A, et al. SUV of [68Ga]DOTATOC-PET/CT Predicts Response Probability of PRRT in Neuroendocrine Tumors. Mol Imaging Biol. 2015 June: p. 313-8.
59. Al-Ibraheem A, Bundschuh RA, Notni J, Buck AK, Winter A, Wester HJ, et al. Focal uptake of 68Ga-DOTATOC in the pancreas: Pathological or physiological correlate in patients with neuroendocrine tumours? European Journal of Nuclear Medicine. 2011 July; 38.
60. Sahlmann C, Meller B, Bouter C, Ritter CO, Ströbel P, Lotz J, et al. Biphasic 68Ga-PSMA-HBED-CC-PET/CT in patients with recurrent and high-risk prostate carcinoma. European Journal of Nuclear Medicine and Molecular Imaging. 2015 November: p. 898-905.
61. Prasad V, Steffen IG, Diederichs G, Makowski MR, Wust P, Winfried B. Biodistribution of [68Ga]PSMA-HBED-CC in Patients with Prostate Cancer: Characterization of Uptake in Normal Organs and Tumour Lesions. Molecular Imaging and Biology. 2016: p. 428-436.